



UPPSALA  
UNIVERSITET

*Digital Comprehensive Summaries of Uppsala Dissertations  
from the Faculty of Science and Technology 1036*

# Emittance and Energy Diagnostics for Electron Beams with Large Momentum Spread

MAJA OLVEGÅRD



ACTA  
UNIVERSITATIS  
UPSALIENSIS  
UPPSALA  
2013

ISSN 1651-6214  
ISBN 978-91-554-8646-4  
urn:nbn:se:uu:diva-198080

Dissertation presented at Uppsala University to be publicly examined in Sal 2001, Ångströmlaboratoriet, Lägerhyddsvägen 1, Uppsala, Friday, May 24, 2013 at 10:15 for the degree of Doctor of Philosophy. The examination will be conducted in English.

#### **Abstract**

Olvegård, M. 2013. Emittance and Energy Diagnostics for Electron Beams with Large Momentum Spread. Acta Universitatis Upsaliensis. *Digital Comprehensive Summaries of Uppsala Dissertations from the Faculty of Science and Technology* 1036. 75 pp. Uppsala. ISBN 978-91-554-8646-4.

Following the discovery of the Higgs-like boson at the Large Hadron Collider, there is demand for precision measurements on recent findings. The Compact Linear Collider, CLIC, is a candidate for a future linear electron-positron collider for such precision measurements. In CLIC, the beams will be brought to collisions in the multi-TeV regime through high gradient acceleration with high frequency RF power. A high intensity electron beam, the so-called drive beam, will serve as the power source for the main beam, as the drive beam is decelerated in special structures, from which power is extracted and transferred to the main beam. When the drive beam is decelerated the beam quality deteriorates and the momentum spread increases, which makes the beam transport challenging. Dedicated diagnostics to monitor the momentum profile along each bunch train and transverse profile diagnostics will be needed to guarantee the reliability of the decelerator and consequently the power source of the main beam acceleration.

A test facility, CTF3, has been constructed at CERN to validate key technical aspects of the CLIC concept. The beam quality in the decelerator will be investigated in the test beam line, TBL, where several power extraction structures reduce the drive beam energy by up to 55%. At the same time, the single-bunch rms energy spread grows from the initial value of 1% to almost 6%. To monitor the parameters of such a beam is challenging but crucial for the optimization of the beamline. In this thesis we report on progress made on adapting generally used methods for beam profile measurements to the demanding conditions of a wide momentum profile. Two detector technologies are used for measuring transverse profile and momentum profile and we discuss the performance of these instruments, in the view of the large momentum spread and with the outlook towards equivalent beam profile monitors in the CLIC decelerator.

*Keywords:* beam instrumentation, particle beam diagnostic, emittance, particle collider, particle accelerator

*Maja Olvegård, Uppsala University, Department of Physics and Astronomy, High Energy Physics, 516, SE-751 20 Uppsala, Sweden.*

© Maja Olvegård 2013

ISSN 1651-6214

ISBN 978-91-554-8646-4

urn:nbn:se:uu:diva-198080 (<http://urn.kb.se/resolve?urn=urn:nbn:se:uu:diva-198080>)

*"Vi har de allra minsta, de kallas för molekyler.  
Molekylerna, de är rysligt små, de... Ja, de är så  
gräsligt små så det har ni ingen uppfattning om,  
så stor ni är."*

Atomubåtsman Malte Lindeman



# List of papers

This thesis is based on the following papers, which are referred to in the text by their Roman numerals.

- I **High intensity profile monitor for time resolved spectrometry at the CLIC Test Facility 3**  
M. Ovegård, E. Adli, H. H. Braun, E. Bravin, N. Chritin, R. Corsini, A. E. Dabrowski, S. Döbert, C. Dutriat, D. Egger, T. Lefèvre, O. Mete, P. K. Skowronski and F. Tecker  
*Nucl. Instr. and Meth. A, Vol. 683, 11 August 2012, pp. 29-39*
- II **Beam profile monitoring at the test beam line at the Compact Linear Collider test facility 3**  
M. Ovegård, E. Adli, W. Andreazza, B. Bolzon, E. Bravin, N. Chritin, A. E. Dabrowski, S. Döbert, M. Duraffourg, T. Lefèvre, R. Lillestøl and V. Ziemann  
*Submitted to Phys. Rev. Special Topics - Accelerators and Beams*
- III **Effect of large momentum spread on emittance measurements**  
M. Ovegård and V. Ziemann,  
*Nucl. Instr. and Meth. A, Vol. 707, 11 April 2013, pp. 114-119*
- IV **Conceptual design of the post-PETS instrumentation line for CLIC**  
M. Ovegård and V. Ziemann,  
*Submitted as a CLIC Note*
- V **Performance of parabolic and diffusive OTR screens at the CLIC test facility 3**  
M. Ovegård, B. Bolzon, E. Bravin, S. Burger, A. E. Dabrowski, T. Lefèvre and C. P. Welsch  
*Proceedings of the DIPAC'11 conference, Hamburg, Germany 2011, pp. 413-415.*

Reprints were made with permission from the publishers.

# Lista över övriga publikationer

Följande publikationer är inte inkluderade i avhandlingen.

**VI A Multi-TeV Linear Collider Based on CLIC Technology:  
CLIC Conceptual Design Report**

M. Aicheler, P. Burrows, M. Draper, T. Garvey, P. Lebrun, K. Peach,  
N. Phinney, H. Schmickler, D. Schulte and N. Toge (Editors)  
*CERN-2012-007, SLAC-R-985, KEK-Report-2012-1, PSI-12-01, JAI-  
2012-001, Geneva, Switzerland, 2012.*

**VII The CLIC Feasibility Demonstration in CTF3,**

P. K. Skowronski, E. Adli, J. Barranco, S. Bettoni, B. Constance,  
R. Corsini, A. E. Dabrowski, M. Divall Csatari, S. Döbert,  
A. Dubrovskiy, W. Farabolini, O. Kononenko, R. L. Lillestøl,  
T. Muranaka, M. Olvegård, A. Palaia, T. Persson, A. Rabiller,  
R.J.M.Y. Ruber and F. Tecker  
*Proceedings of IPAC2011, San Sebastián, Spain, pp. 1042-1044, 2011.*

**VIII Experimental verification of the CLIC Decelerator with the Test  
Beam Line in the CLIC Test Facility 3"**

R. L. Lillestøl, E. Adli, S. Döbert, M. Olvegård, A. Rabiller  
and G. Sterbini  
*Proceedings of IPAC2012, New Orleans, Louisiana, USA, pp. 1885-  
1887, 2012.*

**IX Production of long bunch trains with 4.5  $\mu\text{C}$  total charge using PHIN  
photo-injector,**

O. Mete, E. Chevallay, M. Csatari, A. Dabrowski, S. Döbert, D. Egger,  
V. Fedosseev, M. Olvegård and M. Petrarca  
*Phys. Rev. Special Topics - Accelerators and Beams, Volume 15, Issue  
2, February 17, 2012.*

**X A Segmented Beam Dump for the CTS Line at CTF3,**

M. Olvegård, W. Andreazza, E. Bravin, N. Chritin, A. Dabrowski,  
M. Duraffourg and T. Lefèvre  
*CTF3 Note 103, CERN, Geneva, Switzerland, 2012.*

**XI Spectrometry in the Test Beam Line at CTF3**

M. Olvegård, E. Bravin, F. Carra, N. Chritin, A. E. Dabrowski,  
A. Dallochio, S. Döbert and T. Lefèvre  
*Proceedings of IPAC'10, Kyoto, Japan, pp. 1113-1115, 2010.*

- XII Time Resolved Spectrometry on the Test Beam Line at CTF3**  
M. Olvegård, A. Dabrowski, T. Lefèvre, S. Döbert and E. Adli  
*Proceedings of DIPAC09, Basel, Switzerland, pp. 257-259, 2009.*
- XIII Transient Beam Loading Compensation in CTF3,**  
A. Dabrowski, S. Bettoni, H. H. Braun, E. Bravin, R. Corsini, S. Döbert,  
C. Dutriat, T. Lefèvre, M. Olvegård, P. K. Skowronski and F. Tecker  
*Proceedings of LINAC'08, Victoria, Canada, pp. 585-587, 2008.*
- XIV Comprehensive user manual for the phase-coding system setup and operation with PHIN including the measurements performed with the beam**  
M. 'Csatari' Divall, A. Andersson, B. Bolzon, E. Bravin, E. Chevallay,  
S. Döbert, A. Drozdy, V. Fedosseev, C. Hessler, T. Lefèvre, S. Livesley,  
Ö. Mete, M. Olvegaard and A. N. Rabiller  
*CTF3 Note 101, CERN, Geneva, Switzerland, 2012.*

## My contribution to the papers

**Paper I:** I performed all of the FLUKA simulations and made the analysis to compare the result with the GEANT4 simulations. I participated in most of the measurements and analyzed the data they resulted in. The design of the most recent segmented dump was led and coordinated by me. Of two other segmented dumps I took part in the commissioning. The writing was shared between myself and two other authors and I finalized the accepted version.

**Paper II:** I was responsible for the design, installation and commissioning of the segmented dump. For this I performed FLUKA simulations, and part of the PLACET simulations. I participated in all of the beam measurements and made most of the analysis. Calculations in MATLAB of OTR light were made by me. The work on chromaticity in quadrupole scans was shared between me and the last author, where I made the numerical calculations. Most of the writing was done by me.

**Paper III:** The work was shared between myself and the other author, where I made all the numerical calculations.

**Paper IV:** The work was shared between myself and the other author, where we together developed the measurement strategy. I performed all the numerical calculations and did most of the writing.

**Paper V:** For this paper I performed all the measurements either myself or with the help of others. I handled all the data analysis and the writing.



# Contents

1	Introduction .....	11
1.1	Physics motivation .....	11
1.2	The Standard Model and beyond .....	12
1.3	Particle colliders .....	13
2	CLIC .....	17
2.1	CLIC layout .....	17
2.2	The drive beam .....	19
3	CTF3 .....	23
3.1	Goal and layout .....	23
3.2	Drive beam generation .....	24
3.3	The Test Beam Line .....	26
4	The basics of beam physics .....	29
4.1	Beam parametrization .....	29
4.2	Beamline representation .....	30
4.3	Acceleration and deceleration .....	32
5	Beam profile diagnostics .....	35
5.1	Transverse profile .....	35
5.2	Momentum distribution .....	38
6	Instrumentation .....	43
6.1	Segmented beam dump .....	43
6.2	OTR screens .....	49
7	The post-PETS line .....	57
7.1	Time-resolved spectrometry .....	57
7.2	Time-resolved beam size measurements .....	60
8	Conclusion .....	63
9	Sammanfattning på svenska .....	65
10	Abbreviations and acronyms .....	71
	References .....	77



# 1. Introduction

This thesis covers the development of particle beam diagnostics for a future particle collider. As such, it touches both the field of fundamental particle physics and the more applied area of particle accelerators and instrumentation. The particular research contribution lies within profile monitoring for beams with large momentum spread.

Before we look into the details of this research progress we will provide the background to the field, including basic accelerator physics and beam diagnostic methods. First, we will discuss the motivation for building particle colliders by forming an overview of particle physics of today.

## 1.1 Physics motivation

All matter in the universe, all that we can see or touch, is composed of atoms. Each atom consists of a cloud of electrons surrounding a nucleus, which in itself is composed of a combination of protons and neutrons. How many of each constituent depends on the type of atom, and the combination of atoms defines the final material; an element or a compound. While the electron, as far as we know, is an elementary particle that cannot be divided into even smaller parts, the nuclear particles are formed by three quarks each. This is as far as we can zoom in on matter, but the world of elementary particles does not end here. There is a zoo of other particles that have been observed directly or indirectly, if even for a very short moment. The quest for finding all such building blocks of nature and studying how they interact with each other is the core of particle physics.

In our endeavors we use the smallest imaginable pieces to try to explain everything that happens around us. For every successful experiment we obtain another piece of the giant puzzle that forms the blueprint of the universe and of the laws that govern it. The goal is to create a mathematical and phenomenological model that fits with that blueprint and that can efficiently predict all sorts of physics processes that we observe. There are many such models, some complementary to and some competing with each other. The perhaps most popular and well established is called the Standard Model (SM) and will be described briefly in the next section.

		Generation			Gauge bosons
		I	II	III	
quarks		<b>u</b> up	<b>c</b> charm	<b>t</b> top	
		<b>d</b> down	<b>s</b> strange	<b>b</b> bottom	
leptons		$\nu_e$ electron neutrino	$\nu_\mu$ muon neutrino	$\nu_\tau$ tau neutrino	
		<b>e</b> electron	$\mu$ muon	$\tau$ tau	
					$\gamma$ photon
					$Z^0$ Z boson
					$W^\pm$ W boson
					$g$ gluon

Figure 1.1. The particles included in the standard model, separated into generations and flavors.

## 1.2 The Standard Model and beyond

In physics we separate the interactions between particles into four forces: a) gravitation, b) electromagnetism, c) the weak nuclear force, and d) the strong nuclear force. The SM involves the last three forces while neglecting the first.

Also, the fundamental particles are categorized into groups and types, where the response to the mentioned forces vary from type to type. The SM recognizes 24 fundamental particles. Six of them are leptons, i.e. *light* particles, another six are quarks and the other 12 are gauge bosons. These bosons are the force carriers of the three forces included in the SM, which means that they are responsible for the interaction between the other 12 particles. Figure 1.1 shows the SM particles arranged into a “periodic table” of elementary particles, where the forces are present through the corresponding boson: photon,  $\gamma$ , for the electromagnetic interaction, 8 gluons,  $g$ , for the strong interaction, and the  $W^\pm$ - and the  $Z^0$ -bosons for the weak interaction. In addition, every particle except the bosons has an antiparticle. Leptons respond only to the electromagnetic and the weak (under certain conditions unified under the name electroweak) interactions, while hadrons, that consist of quarks, are affected also by the strong interaction.

Apart from a list of elementary particles, the SM model offers a framework for calculating physical properties and processes which agrees with observations with remarkable accuracy. However, there are dark areas also on the SM map. For example, the seemingly basic property of mass cannot be explained through the interactions and particles above. In other words, there is no mechanism in the SM that explains why particles of otherwise equal or similar properties have so different rest masses. In the 1960s theoreticians developed

a mathematical model that would predict the mass symmetry breaking. In this model yet another boson would give the particles this property and it has since then been called the Higgs boson after one of the founders of the theory [1].

Although, the SM together with the Higgs mechanism would be a nearly complete model of the world we can see, it still lacks explanation force on other aspects. There are many free parameters that cannot be derived from fundamental principles in the SM. Neither does it predict the existence of dark matter, the existence of which has been established through astronomical observations [2]. Thus, new theories and models, covering the physics beyond the SM have been developed. One of these models is the Supersymmetry (SUSY) theory, which predicts that dark matter consists of subatomic particles called supersymmetric particles, or *sparticles*. Every known particle would then have a supersymmetric partner particle that is so heavy that no experiment so far have been able to see it [2].

Another riddle still to be solved is the asymmetry between matter and antimatter. An experiment designed to precisely measure a slight asymmetry in certain particle decays, might be able to explain the surplus of matter over antimatter in the world. The baffling attributes of neutrinos, the possible existence of extra dimensions, the unification of forces at very high energies, are other mysteries that the particle physics community wants to investigate.

To probe these small particles we need to reach a wavelength of the order of the de Broglie wave length of the object. Shorter wavelength means higher particle energy and we reach a high energy in the center of mass frame more efficiently by colliding two beams than by impinging one beam on a fixed target.

### 1.3 Particle colliders

If the goal of particle physics is to probe the building blocks of the universe, then the means to do it is particle colliders. In a particle collider we accelerate particles to speeds near the speed of light in vacuum by letting them interact with electromagnetic radio-frequency (RF) waves in special accelerating structures, or cavities. The particles travel in bunches and a string of bunches form a beam. Once the beams have reached the desired energy they are brought into collision. At the collision point the energy density is so high that it can materialize and form new particles. The tracks of these particles and of their decay products are recorded by large particle detectors surrounding the interaction point. Many events occur at every beam collision and new particles and phenomena are hidden among the traces of particles that have already been discovered. The data taken with these detectors often take several years to analyze, using complicated algorithms and selection criteria to uncover potential discoveries from a dominating background.

This is for example how the last quark, the top quark  $t$ , was discovered in 1995 at the Tevatron proton-antiproton collider [3, 4]. The aim of the largest particle collider at present, The Large Hadron Collider (LHC) at CERN, is to verify the existence of the Higgs mechanism and to explore physics beyond the Standard Model.

## The LHC and its successor

In LHC two beams of protons are accelerated in a circular machine so that the energy is ramped up turn by turn before they are brought to collide at four interaction points, each surrounded by a large detector system. Two of these, ATLAS and CMS, are specialized in the search for the Higgs boson and supersymmetric particles. A third, ALICE, has been designed to study quark-gluon plasma produced in heavy ion collisions, while the fourth, LHCb, is dedicated to investigating the asymmetry between matter and antimatter through the decay of beauty quarks. The beams will soon collide at a center-of-mass energy of up to 14 TeV, more than 14 thousand times the energy of a proton at rest. Through the high energy collisions, doors are opened towards exciting new physics, both within and beyond the Standard Model. Protons are ideal ingredients for the discovery of new particles. Because they are stable and therefore abundant in nature they are relatively easy to cluster into a beam, and, due to their hadronic nature, they couple mostly through strong interaction, through which many processes are more likely to occur. In particular, they are heavy and can thus reach high energies easier than lighter particles.

One of the main goals of the LHC was to find the Higgs particle and in June 2012 evidence of a new boson was announced. Though, until today it is not clear whether the found boson fits into the SM description of the Higgs particle, so further analysis is ongoing [5].

There were of course other motivations for constructing such an expensive and complex machine as the LHC. The SUSY model, and various varieties of the same, also include Higgs-like bosons called non-SM Higgs, some of which are charged [6]. There is hope of finding traces of these particles in at least one of the four main experiments at the LHC. In addition, probing extra dimensions, and understanding the asymmetry between antimatter and matter are scientific targets of the LHC experiments.

Already before the LHC has reached its nominal performance, there are activities surrounding the life after LHC of particle physics in general and of colliders in particular. Once new discoveries have been made, more precise measurements are needed, e.g. to find the exact mass and couplings of the Higgs boson. For this task protons do not serve us well since they are composite particles, but we need elementary particles as projectiles. The reason is that in a proton-proton collision it is actually the quarks and gluons that interact with each other. And since the quarks themselves carry part of the

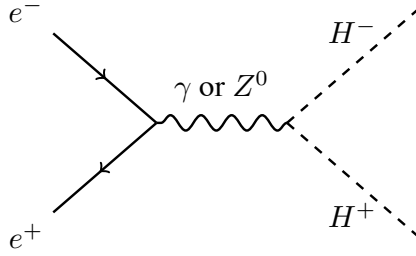


Figure 1.2. An example of production of a pair of charged Higgs bosons in an electron-positron collider.

total energy held by the proton, the energy resolution of the experiment will be limited by the internal energy distribution.

Only with beams of fundamental particles can a future collider perform the desired precision measurements. In reality that implies the use of leptons since quarks have never been observed as free particles but only in bound states with other quarks. For practical reasons electrons and positrons are the best option since they are relatively easy to isolate into beams. However, other options are being studied, like e.g. a muon collider [7, 8]. Though, the difficulty of making muon beams small enough to meet the requirements of a lepton collider, is pushing this particular option into the more remote future. Furthermore, we can profit from thorough knowledge on colliding electrons and positrons since there are several electron-positron colliders still active. e.g. DAFNE in Italy, whereas some, like the Large Electron-Positron Collider, LEP, have retired.

The future  $e^+e^-$  collider will act as a complement to the LHC. This means that the required collision energy will be predominantly set by the discoveries made in the LHC. Until it is known we can only speculate and study the physics potential at different energies. Though, a general agreement is that the TeV regime will need to be covered [9] in order to access physics beyond the Standard Model.

An example of a physics event in an electron-positron collider is the production of a charged-Higgs pair, illustrated in Fig. 1.2 with a Feynman diagram showing the direct production of two Higgs particles. Charged Higgs bosons are predicted by e.g. the Minimal Supersymmetric Extension of the Standard Model (MSSM) and can be produced via a virtual  $\gamma$  or  $Z^0$ . The short-lived Higgs bosons decay to other particles with branching ratios that will remain unknown until the MSSM parameters, such as the charged-Higgs mass, are known. Possible decay channels are e.g. a leptonic decay to  $\tau \nu_\tau$  or a hadronic decay to  $t\bar{b}$  [10]. These particles decay to other particles that are recorded in the particle detectors surrounding the interaction point. With a lepton collider the event is “cleaner”, since the full center-of-mass energy goes to the production of the charged Higgs bosons, while in a hadron collider the Higgs will spring out of mainly gluon-gluon interaction. In addition, the illustrated event suffer less from a background of hadronic showers.

## A linear $e^+e^-$ collider for the future

A charged particle that is accelerated emits electromagnetic radiation [11]. For relativistic particles the energy loss is negligible when the acceleration is along the direction of motion. If, however, the acceleration occurs perpendicularly, the radiated power can be substantial. The energy loss per turn  $\Delta E$  of a particle of rest mass  $m$  and energy  $E$  in a ring of radius  $\rho$  is proportional to [12]

$$\Delta E \propto \frac{E^4}{m^4 \rho}. \quad (1.1)$$

We note that for a given energy we need to use heavier particles or a machine of larger radius in order to reduce the energy loss due to synchrotron radiation. Protons are almost two thousand times heavier than an electron, which is why the LHC could replace LEP in the already existing 27 km circumference tunnel at CERN. In reality it is impractical to build a circular collider even larger than the LHC. From a cost point of view it is actually more effective to reach the TeV regime with a linear collider.

With a linear collider we avoid energy losses due to synchrotron radiation, as discussed above. On the other hand we get only one chance to reach the top energy before the beams are brought into collision, so that we sacrifice the turn-by-turn reuse of accelerator equipment and beam particles. However, another advantage of a linear collider is that it facilitates energy scans, where the collision energy is changed in steps in order to turn on and off physics processes. Another advantage is that it can be constructed in stages and thus be successively upgraded to higher energies.

According to the European committee for future accelerators (ECFA) a future lepton collider should reach at least 0.4 TeV, 0.2 TeV per beam, and a luminosity of at least  $10^{34} \text{ cm}^{-2} \text{ s}^{-1}$  [9]. The luminosity is a quality measure of a collider. It gives the probability of interactions to occur and sets a time scale during which the machine has to be operational. The higher the luminosity, the shorter time a certain measurement will take. In other words, a future collider should strive at providing as high luminosity as possible.

The accelerator complex that we discuss here are immense projects and imply an international effort in terms of labor and financial contribution. One wishes to reduce the construction and operation costs to a minimum and to keep the power consumption as low as possible. There are two major ongoing projects for a linear collider that both meet the requirements on energy, luminosity and power consumption, but through different choices of technology. One is the International Linear Collider (ILC), which is based on superconducting technology, and aims at a collision energy of 0.5 TeV. The other is the Compact Linear Collider (CLIC) study, conducted at CERN. It aims at six times higher center-of-mass energy (3 TeV) using normal-conducting technology. Since the work discussed in this thesis is specific to CLIC, we will devote the next chapter to describing CLIC and its main technical challenges.



## 2. CLIC

The Compact Linear Collider, CLIC, is a project for a future linear  $e^+e^-$  collider. It will bring the beams to a collision energy of 3 TeV, with a luminosity of  $5.9 \cdot 10^{34} \text{ cm}^{-2} \text{ s}^{-1}$  [13]. Thus, it fulfills the goals put up by ECFA and will in that way be able to perform precision measurements on phenomena discovered at LHC, like for example determining the exact mass and quantum numbers of the newly discovered boson, and of supersymmetric particles. The CLIC study is an international effort with collaborators from more than 40 institutes located in over 20 different countries. The work is coordinated by CERN in Switzerland, which is also a possible final location for the 48 km collider.

In CLIC, the beams are accelerated with high gradient structures, which implies that it is a relatively compact machine for a given energy. Using superconducting accelerating cavities is not an option because they are limited in gradient to about a third of what is achievable with normal-conducting cavities, which are therefore used in CLIC. These high accelerating gradients imply that very strong electromagnetic fields are present, and the desired luminosity can only be reached if the beam intensity is high. Then, delivering the required RF power to the acceleration structures along the long linac becomes a challenge. Instead of using conventional RF sources, klystrons, CLIC relies on a novel two-beam acceleration concept, where initially the power is stored and transported in an electron beam of high intensity. RF power is extracted from this high intensity, medium energy beam, referred to as the drive beam, and fed to the main beam of medium intensity running in parallel. As the drive beam is decelerated, it provides acceleration RF for the main beam, which reaches the TeV regime before collision.

Paper VI contains an extensive description of the CLIC project. In this chapter we will discuss the main characteristics of CLIC and the two-beam acceleration scheme. In particular, we will have a look at the high intensity drive beam, which is an essential part of the CLIC RF source.

### 2.1 CLIC layout

Figure 2.1 presents a schematic layout of the CLIC complex, with its quartet of accelerator complexes: the two drive beam complexes, the electron main beam and the positron main beam. Each drive beam begins with a thermionic electron gun, where the electron bunch trains are generated [14]. The drive

beam linac that follows accelerates each beam to 2.4 GeV, which is its final energy. It is then subject to a sophisticated pulse compression scheme in order to become the high intensity, high frequency drive beam needed to maximize the energy transfer to the main beam. This takes place in the delay loop and the two combiner rings, where bunches are interleaved and recombined so that the originally long bunch train is transformed into a short bunch train with several times the original bunch frequency and average intensity. After the bunch train compression, the drive beam makes a turnaround and is injected into decelerator sectors. Here, the beam is decelerated until 90% of the beam power has been extracted, and then dumped. From each decelerator the extracted energy is transferred to the main beam for acceleration.

The main beam setup begins equally with an electron gun, or with a more complicated positron source. Each main beam goes through a first acceleration stage in the injector before it enters a pre-damping ring and a damping ring. These rings are present for a controlled reduction of the beam dimension through the emission of synchrotron radiation. Ultra-small sizes are needed for high luminosity and efficient collisions, and need to be preserved throughout the remaining beamlines. After the damping rings, the main beams enter a common booster linac, which brings their energy to 9 GeV. Behind a turnaround, the main linac follows. The main linac runs in parallel with the drive beam decelerators so that the power extracted from the drive beam can be fed directly to the main beam acceleration structures. Not visible in the sketch is the post-collision beamlines which finally take the spent beams safely away from the interaction point (IP) [15].

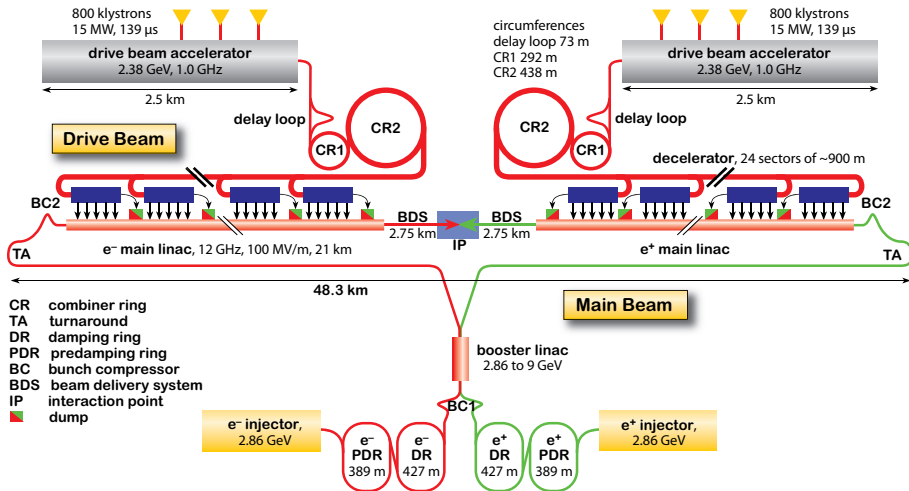


Figure 2.1. A layout of the CLIC complex [16], with the drive beam generation at the top and the main beams below.

## 2.2 The drive beam

The high accelerating gradient was chosen in order to make the accelerator compact, as mentioned earlier. However, a high accelerating gradient means a strong accelerating field, which reduces the efficiency of the power transfer from the RF wave to the beam. This efficiency is on the other hand improved again if the RF frequency is high [17]. As a compromise between accelerator compactness and power consumption CLIC will run at 100 MeV/m accelerating gradient and with 12 GHz RF frequency. With the beam intensity foreseen for CLIC, this means a challenge in terms of power production. At least 35 000 klystrons per accelerator, at 50 MW each, would be required, together with stages of pulse compression to reach the desired frequency and power. Though feasible it is not practical to use conventional RF sources, klystrons, which is why the two-beam acceleration scheme will be employed. Here, the drive beam acts as an RF source, which is expected to be more efficient and cost effective, but requires a complex rearrangement of the bunches in the drive beam.

Since we want the acceleration RF to be a 12 GHz wave, the drive beam that will provide it needs to have a density variation that peaks strongly at 12 GHz. In other words, the drive beam will have a 12 GHz bunch frequency. In addition, the peak power of the extracted RF power needs to be high, which calls for a high average current and high bunch charge in the drive beam. The high bunch charge, listed in Table 2.1, is achieved directly at the source, whereas the 12 GHz bunch frequency requires a complex system of bunch structure manipulations where the bunch spacing is reduced in steps. This takes place in the delay loop and the combiner rings where bunches are carefully interleaved so that the initially long bunch train is compressed to a short train where the bunches are more densely spaced. An amplification of the average beam intensity along the train occurs in the same process, and guarantees an efficient power generation when the drive beam is decelerated.

Instead of preparing a bunched electron beam in every klystron, the drive beam is prepared centrally and then decelerated in the power extraction and transfer structures (PETS) which have the role of the out-coupling cavity in a klystron. The PETS are distributed along the main beam linac so that they, together with the drive beam, function as a distributed klystron. As a consequence, the behavior of the drive beam determines the stability and the availability of the whole collider complex. This implies that the drive beam needs to be well understood and controlled at every step, which calls for dedicated beam diagnostics. Compared to the main beam, the drive beam has special characteristics, where the unusually high intensity and the short bunch spacing are two of the challenges for diagnostics. Table 2.1 presents a comparison of the beam parameters of the main beam just before collision, the drive beam after acceleration but before pulse compression, and the drive beam after the deceleration.

**Table 2.1.** Beam parameters of the main beam before collision (MB), of the drive beam just before pulse compression (DB a) and after deceleration (DB b) [13].

Parameter	Symbol	unit	MB	DB a	DB b
Energy	$E$	GeV	1500	2.37	0.237
Intensity	$I$	A	1.2	4.2	101
Bunch charge	$Q_b$	nC	0.6	8.4	8.4
Bunch frequency	$f_b$	GHz	2	0.5	12
Bunch train duration	$\Delta t$	$\mu\text{s}$	0.156	140	0.240

In the drive beam decelerator up to 90% of the energy is extracted from the beam. At the same time as the average momentum decreases, the momentum spread grows substantially. The initial energy spread of 1% rms increases up to almost 40%. In addition, the energy profile takes an asymmetric form with a long high-energy tail, extending all the way to the initial energy. With such an energy distribution, illustrated in Fig. 2.2, the transport of the beam through the on average 877 m long decelerators is a very challenging task and the beam dynamics of the decelerated beam becomes critical. Extensive beam diagnostics is needed to supervise the beam evolution in and after the decelerator. In particular, the momentum distribution along each bunch train needs monitoring and emittance measurements are required to assure a low level of particle losses. Ultimately, the instruments that will supervise the behavior of the drive beam are there to guarantee that stable, high power RF can be delivered to the main beam.

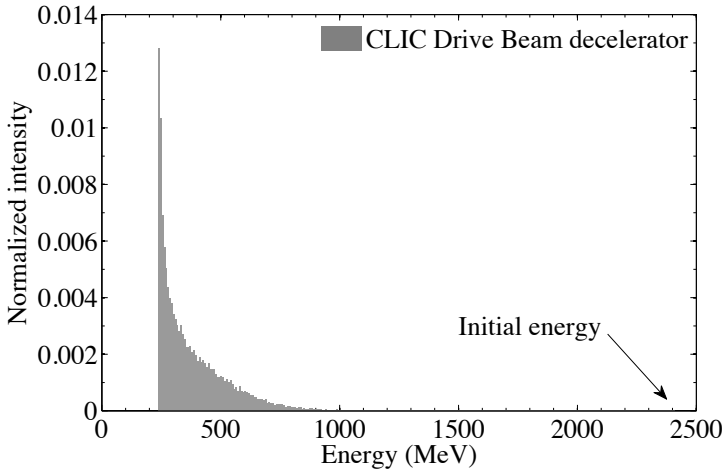


*Figure 2.2.* The energy distribution of a fully decelerated nominal drive beam. While the majority of the particles are decelerated to a minimum of 240 MeV, the high energy transient has particles up to the initial energy of 2.4 GeV.

Incidentally, this novel and advanced design for a collider caused the identification of a number of critical feasibility aspects, identified in 2003 by an international panel employed to review the CLIC project. The panel discerned five critical technical challenges that needed further study in order to verify the feasibility of the project [18]. These points are listed below:

1. Design of high frequency accelerating structures with wakefield damping, for high gradient acceleration.
2. Validation of the drive beam generation scheme with fully loaded operation of the drive beam linac.
3. Design and test a structure for power extraction with on/off capability.
4. Validation of beam stability and losses in the drive beam decelerator.
5. Test with beam of a two-beam acceleration module for the main linac (now called CLIC module).

For this particular purpose a test facility has been built at CERN by an international collaboration. The facility addresses some of these aspects, with an emphasis on the CLIC RF source with drive beam generation, substantial deceleration of the same, and of two-beam acceleration. We will here focus on the beam profile measurements of the decelerated beam (summarized in Paper II) in the beamline where item 4 is addressed: Experimental tests of the drive beam decelerator. The next chapter will be dedicated to the description of the test facility, before we continue to look at the beam diagnostics.



### 3. CTF3

The CLIC project includes many technical challenges, some of which require substantial research and development on accelerator equipment and methods beyond the state-of-the-art. In order to show proof-of-principle of central aspects of CLIC, a test facility, CTF3, was constructed at CERN. This chapter describes the goal, layout and key features of the CLIC test facility.

#### 3.1 Goal and layout

CTF3 [19] has been constructed to experimentally address a number of central aspects of the CLIC complex, that were listed at the end of the previous chapter. As a first step, acceleration with full beam loading was demonstrated in 2004 [20]. After completing the construction of delay loop and combiner ring, in 2009 [21], a high current, high intensity drive beam was successfully generated using the sophisticated manipulation scheme, thus completing the task of the second item on the list. High-power RF production through repeated deceleration of the drive beam is currently being studied to address item 3, and using the extracted RF power for acceleration at a gradient above 100 MeV/m, item 1, was done successfully in 2010 [22]. Recent progress in CTF3 is reported in Paper VII.

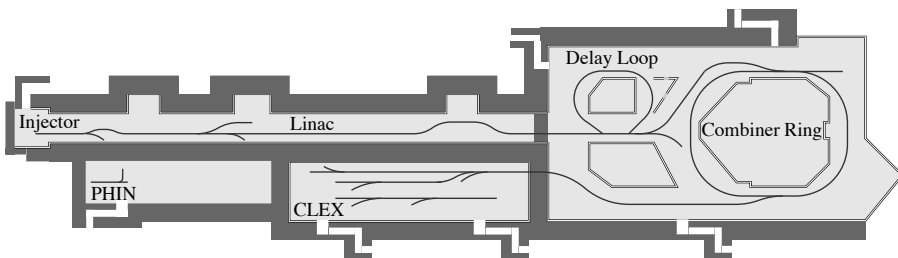


*Figure 3.1.* A layout of the CTF3 complex.

The CTF3 complex, presented with a sketch in Fig. 3.1, consists of three main sections: (a) a linear accelerator, (b) a delay loop followed by a combiner ring, and (c) an experimental area, named CLEX. The beams are produced by an injector [23] consisting of a DC thermionic gun, a 1.5 GHz subharmonic buncher, a 3 GHz bunching system and two 3 GHz accelerating structures. The injector accelerates the beam of nominal intensity 4 A up to roughly 20 MeV.

Following the injector, there is a 70 m long linac composed of 14, 3 GHz accelerating cavities operated in fully loaded mode, thus addressing point 2 on the list of feasibility issues. At the end of the linac the beam has reached its highest energy of 150 MeV.

The delay loop and the combiner ring are utilized for the manipulations of the bunch structure, by interleaving and recombining bunches, in order to compress the  $1.2\ \mu\text{s}$  bunch train into the desired drive beam with a bunch spacing of 2.5 cm corresponding to 12 GHz, and a pulse train duration of 140 ns. The generation of the drive beam is crucial for maximizing the power transfer from the drive beam to the main beam and is the second main part of item 2 in the list of technical feasibility issues.

When the bunch train has been compressed it is transported to CLEX, which has three beam lines: the test beam line (TBL) (Paper VIII) targeting item 3, the two-beam test stand (TBTS) and Califes [22] where item 1 and eventually item 5 are covered. In the TBTS, the drive beam is decelerated in one PETS. The extracted power is fed to another electron beam running in parallel. This moderate intensity probe beam of 1 A (0.6 nC bunch charge), is injected from Califes at approximately 180 MeV, with 1.5 GHz bunch frequency, and simulates the main beam in the CLIC two-beam acceleration. With a single PETS, the deceleration is small, wherefore beam stability is not an issue. In TBL, however, the deceleration takes place in a sequence of PETS and the energy loss of the beam is substantial. In this case, the beam dynamics becomes critical, which calls for dedicated beam diagnostics.

In addition to mentioned areas, there is the photo-injector test PHIN in a separate hall adjacent to the rest of the accelerator. The PHIN activities are discussed in Paper IX.

## 3.2 Drive beam generation

The CTF3 injector produces a long bunch train with 1.5 GHz bunch frequency while the frequency of the accelerating RF is 3 GHz, i.e. twice the bunch frequency. Every area in the RF phase space where stable acceleration can take place is called a bucket. In the linac there is, in other words, a bunch in every other RF bucket. The bunch rearrangement strategy that takes place in the delay loop is illustrated in Figure. 3.2. An essential ingredient to these manipulations is a fast switch of the RF phase in the subharmonic bunching system. A 180 degrees switch occurs every 140 ns in the  $1.2\ \mu\text{s}$  long bunch train, and thus a part of the bunch train, represented by the black dots, is shifted one RF period compared to the previous 140 ns, marked with white dots in the upper right part of Fig. 3.2. The bunches are equally accelerated by the 3 GHz RF in the linac, with the shifted bunches (black dots) positioned in the odd RF buckets and the non-shifted bunches in the even buckets (white dots). As the beam reaches the delay loop it passes through a transverse deflecting cavity,



operating at 1.5 GHz. The arrival of the beam is synchronized with the deflector so that the bunches in the even buckets are injected to the delay loop while the bunches in the odd buckets bypass the loop. More precisely, every second portion of the bunch train is injected into the delay loop while the other continues straight, as shown in Fig. 3.2. The length of the delay loop is adjusted through a wiggler magnet so that the bunches are recombined at the exit with exactly 180 degrees distance. In this way, the delay loop transforms the 1.2  $\mu$ s pulse bunched at 1.5 GHz into 140 ns long sub-pulses with twice the bunch frequency. A similar procedure occurs in the combiner ring, so that the 140 ns bunch trains are recombined with each other at a 90 degrees phase shift from bunch to bunch until they form a single 140 ns bunch train with 8 times higher average pulse current and bunch frequency.

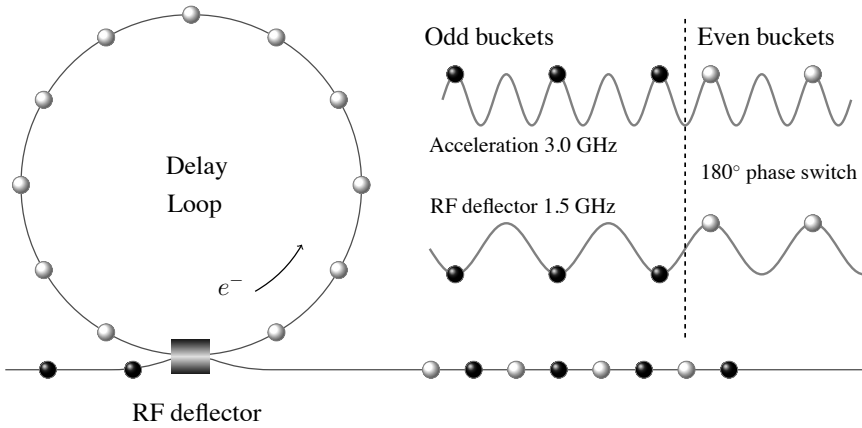


*Figure 3.2.* Bunch frequency multiplication scheme in the delay loop.

An important feature of the CTF3 drive beam complex is that it can be operated in different configurations. Firstly, the injector can deliver either the nominal 1.5 GHz beam or a 3 GHz beam at half the nominal bunch charge. With the latter it is possible to bypass the delay loop and send the beam directly to the combiner ring. There, a 12 GHz beam, but at half the nominal current, is generated. It is equally possible to bypass also the combiner ring or to extract the beam from the ring after a given number of turns. Thus, there is a wide variety of beam currents that can be transported to CLEX for experiments. This is important since the RF power production depends directly on the beam current.

The high frequency high intensity drive beam is transported to CLEX, shown in Fig. 3.3. In CLEX, the use of the drive beam is shared between two experiments: the deceleration studies in TBL and the two-beam acceleration tests in TBTS. TBTS has a single PETS equipped with power recirculation for power build-up in the structure, and with an on/off mechanism. The PETS powers two 12 GHz accelerating structures which, when the PETS is in on-mode, are filled with power extracted from the drive beam and accelerate the probe beam

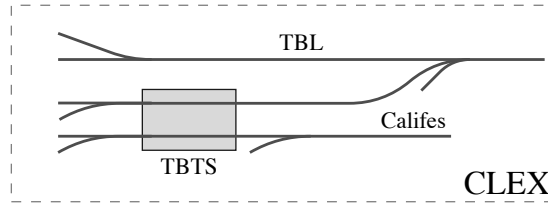


Figure 3.3. A close-up on the CLEX area with the test beam line and the two-beam test stand, behind the probe-beam injector Califes.

with over 100 MeV/m. The studies in TBTS are focused on the high gradient acceleration of the probe beam, including RF breakdowns in the structure and resulting kicks to the probe beam [24]. The single PETS in TBTS causes little deceleration to the drive beam wherefore the beam dynamics is a less critical issue. This can be placed in contrast to the situation in TBL where several PETS are employed for a substantial deceleration of the drive beam. Here, the momentum decrease is significant and its effect on the beam stability needs special care and attention.

### 3.3 The Test Beam Line

The test beam line has been constructed to be a small-scale version of the CLIC drive beam decelerator [25, 26]. Just like the CLIC decelerator, it consists of a simple FODO lattice of alternating focusing and defocusing elements which is a standard configuration of quadrupole magnets. Between magnets there is a PETS. There are 8 FODO cells, allowing for 16 PETS in total, of which 13 have been installed. Each quadrupole in the FODO lattice is mounted on a precision mover [27], allowing for dispersion-free steering and other beam-based alignment techniques. A beam position monitor (BPM), is mounted right behind each quadrupole to measure horizontal and vertical beam position and beam intensity. A sketch of the TBL layout is presented in Fig. 3.4, showing also the two diagnostic sectors that are employed for beam profile measurements before and after deceleration.

TBL targets the study of the drive beam when subjected to heavy deceleration, with the final goal of verifying that stable beam and stable RF power extraction can be maintained simultaneously. A special PETS was designed for TBL to generate the same amount of power as the nominal PETS in the CLIC design, considering the difference in some of the drive beam parameters, in particular the lower beam current. Each PETS produces 140 MW of power at nominal beam current and decelerates the beam by 5.2 MeV. This implies that in the nominal configuration with 16 PETS, 55% of the beam energy will be extracted as the beam is decelerated from 150 MeV to 67 MeV. Due to the filling time of the PETS, there is a 3 ns long high-energy transient

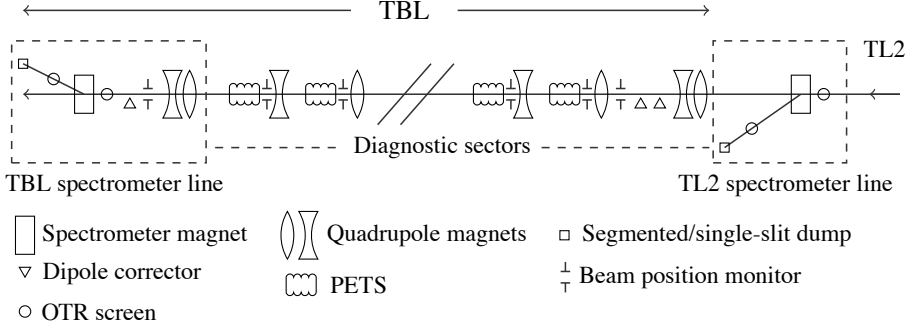


Figure 3.4. The layout of the test beam line. The beam enters from CTF3 from the right.

followed by a long steady state, as depicted in Fig. 3.5. The figure is an example taken from Paper II and shows the beam energy at the end of the line during the first 10 ns of the 140 ns beam pulse, or equivalent, bunch train, simulated in PLACET [28, 29]. As the beam is decelerated, the energy spread grows rapidly from 1% (rms) to near 6%. The large energy spread is obvious in the energy histogram in figure 4 in Paper II, where we also see that there is a substantial high energy tail with particles all the way up to the initial energy.

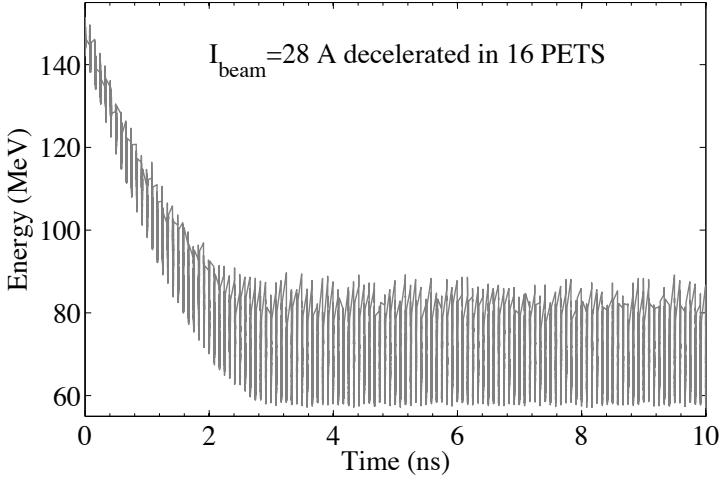


Figure 3.5. A PLACET simulation showing the beam energy distribution in TBL as a function of time during the first 10 ns of a 28 A beam pulse, initially at 150 MeV, decelerated in 16 PETS. The 3 ns long high-energy transient is followed by a 137 ns steady state with an unusually large energy spread.

Since the main objective of TBL is the study of how repetitive RF power extraction affects the beam, the extracted power is only measured at the output of each PETS and not used for acceleration. However, measuring the extracted

power is important, since the ultimate goal is to produce stable power while keeping the drive beam under control. For the latter, beam diagnostics is essential since the large momentum spread is a challenge for the beam stability and because a constant high beam intensity is important for the power production. Apart from the beam current, the transverse properties of the beam are measured, in order to optimize the set-up of the decelerator and to avoid particle losses. Furthermore, the momentum spectrum of the beam needs supervision since it provides understanding of how the power extraction affects the beam. With information about the momentum spectrum along a single bunch train we can tune the beam and the accelerator to stably provide power. The requirement of a measurement of the momentum spectrum along each bunch train triggered the development of a time-resolved spectrometer for TBL. This device is treated in Paper II, together with the other beam profile monitors in TBL.

The next chapters will be dedicated to the physics and the diagnostics of particle beams, with an emphasis on dealing with beams with large momentum spread, having TBL and the CLIC drive beam decelerator in mind.

## 4. The basics of beam physics

Before we go into the physics and methods of beam diagnostics we need the basic tools for describing a particle beam. This chapter will therefore provide the framework of accelerator physics, and describe how a beam is parametrized mathematically, how it is treated in a physical beamline, and finally the fundamentals of particle acceleration and deceleration.

### 4.1 Beam parametrization

To describe a beam particle in a convenient way we first define an ideal particle path through the physical beamline, consisting of magnets, drift spaces, instrumentation, and other components. Generally, the ideal path goes through the center of all magnets and devices. A particle's deviation from this ideal path in a tangential system is then the quantity that is used [12]. The position along the beamline is generally denoted  $s$ . In the transverse plane we use  $x$  for the horizontal deviation and  $y$  for the vertical deviation from the ideal path. Each particle also has a direction, which is related to its momentum in the transverse plane  $p_{x,y}$ , normalized to its momentum in the forward direction  $p$ . The transverse direction can be further divided into a horizontal direction, or angle,  $x' = p_x/p$  and a vertical angle  $y' = p_y/p$ . At a given position in the beamline we use the arrival time of a particle to represent the longitudinal, or equivalently the temporal, position of a particle with respect to the ideal. The last parameter is the energy or momentum of the particle. Also in this case we use the deviation from the ideal or average by introducing  $\delta = \Delta p/p_0$ , where  $\delta$  is the momentum deviation normalized to the reference momentum  $p_0$ . We now have six parameters  $(x, x', y, y', t, \delta)$  to describe any particle in the beamline. It is often possible to assume that the two transverse dimensions of the beam are decoupled, so that the horizontal and the vertical planes can be considered separately.

When we consider a distribution of beam particles rather than a single particle we introduce the sigma matrix  $\bar{\sigma}$  that contain the second order moment of the beam distribution:

$$\bar{\sigma} = \begin{pmatrix} \langle x^2 \rangle & \langle xx' \rangle \\ \langle xx' \rangle & \langle x'^2 \rangle \end{pmatrix}. \quad (4.1)$$

Just as  $x$ ,  $x'$ , etc. depend on  $s$ , so does  $\bar{\sigma}$ . For distributions of particles it is also common to use Twiss parameters  $\alpha$ ,  $\beta$ ,  $\gamma$ ,  $\varepsilon$  [30], also known as

the Courant-Snyder parameters [31]. An important quantity is the geometric beam emittance  $\varepsilon$ , which is a measure of the volume that the beam occupies in phase space. The beam envelope, i.e. the transverse limit within which a given fraction of the particles appear, is given by  $\sqrt{\langle x^2 \rangle} = \sqrt{\varepsilon \beta}$ . Similarly, the beam divergence is defined by  $\sqrt{\langle x'^2 \rangle} = \sqrt{\varepsilon \gamma}$ , where  $\gamma = (1 + \alpha^2)/\beta$ . That means that the sigma matrix also can be expressed in terms of the Twiss parameters as

$$\bar{\sigma} = \begin{pmatrix} \sigma_{11} & \sigma_{12} \\ \sigma_{21} & \sigma_{22} \end{pmatrix} = \varepsilon \begin{pmatrix} \beta & -\alpha \\ -\alpha & \gamma \end{pmatrix} \quad (4.2)$$

where  $\sigma_{21} = \sigma_{12}$ . We use this fact to determine the emittance through consecutive beam size measurements, as will be explained in the following section.

The relativistic momentum of a particle of mass  $m$  is given by  $p = \beta_r \gamma_r mc$ , where  $\gamma_r$  is the relativistic Lorentz factor and  $\beta_r$  the particle speed in units of the speed of light  $c$ . As the average momentum increases during acceleration, the emittance decreases through adiabatic damping, since  $p_{x,y}$  remains constant and  $p$  grows, and therefore the angles  $x'$  and  $y'$  shrink. So, during the acceleration it is therefore common to use the normalized emittance  $\varepsilon_N = \beta_r \gamma_r \varepsilon$  which remains constant also if the momentum changes. In this thesis we will refer to the geometric emittance, unless explicitly stated otherwise. Conversely, during deceleration the process is reversed and the emittance grows, which makes diagnostics the more important.

## 4.2 Beamline representation

Particle beams have many similarities to optical beams and are treated in a similar way. The most important elements in an accelerator can be represented by a transfer matrix. With this matrix the particle or beam parameters are propagated through the element. This implies that the beam variables  $x, x', \dots \delta$  are small so that we can use the paraxial approximation. For a complete description we need six variables to characterize a beam and consequently a six-by-six matrix to propagate it. However, if the horizontal plane is decoupled from the vertical plane, which is generally the case, those two dimensions can be treated separately. We will ignore the arrival time for a simple illustrating case, which leaves only three variables: horizontal position and direction, momentum, and three-by-three matrices to transform them. We use a simple drift space as an example and start with a single particle at position  $x_0$ , direction  $x'_0$  and momentum  $\delta_0$ . A drift is an empty space with no active elements and is represented by the matrix

$$M_{drift} = \begin{pmatrix} 1 & L & 0 \\ 0 & 1 & 0 \\ 0 & 0 & 1 \end{pmatrix} \quad (4.3)$$

where  $L$  is the length of the drift space. After the drift space the beam coordinates have changed to

$$\begin{pmatrix} x \\ x' \\ \delta \end{pmatrix} = \begin{pmatrix} 1 & L & 0 \\ 0 & 1 & 0 \\ 0 & 0 & 1 \end{pmatrix} \begin{pmatrix} x_0 \\ x'_0 \\ \delta_0 \end{pmatrix} = \begin{pmatrix} x_0 + Lx'_0 \\ x'_0 \\ \delta_0 \end{pmatrix}. \quad (4.4)$$

Another example is a focusing quadrupole, of which the transfer matrix is expressed as

$$M_{QF} = \begin{pmatrix} 1 & 0 & 0 \\ -1/f & 1 & 0 \\ 0 & 0 & 1 \end{pmatrix} \quad (4.5)$$

where  $f > 0$  is the focal length of the quadrupole magnet. For  $f \rightarrow f < 0$  the same matrix represents a defocusing magnet. Note that a quadrupole which is focusing in the horizontal plane acts defocusing in the vertical plane, and vice versa.

Several matrices can be combined to represent an arbitrary portion of the beamline. That is,  $R = M_n M_{n-1} \dots M_1$  where  $M_j$  each represent a given sector or element. Note that  $M_1$  is the matrix representing the first element that the particle encounters. The final particle vector  $u$  is then given by  $u = Ru_0$ , where  $u_0 = (x_0, x'_0, \dots, \delta_0)$  is the vector containing the initial parameters. The sigma matrix is propagated through

$$\bar{\sigma} = R \bar{\sigma}_0 R^t. \quad (4.6)$$

The path of a charged particle moving in a magnetic field is changed depending on the particle momentum. In a dipole magnet, here a rectangular bend, we see the relation directly from the transfer matrix

$$M_B = \begin{pmatrix} 1 & \rho \sin \varphi & \rho(1 - \cos \varphi) \\ 0 & 1 & 2 \tan \frac{\varphi}{2} \\ 0 & 0 & 1 \end{pmatrix} \quad (4.7)$$

with  $\varphi = L_{eff}/\rho$  and  $L_{eff}$  the effective length of the magnet, and  $\rho$  is the bending radius. Note here that the momentum is coupled to the transverse plane so that a dipole magnet acts as a spectrometer. We use the term dispersion function  $D$  as a quantification of how the position of a particle that differs in momentum from the design particle varies throughout the accelerator. The dispersion is a property of the physical beamline rather than of the beam. By definition,  $D(s)$  is the trajectory of a particle with  $\delta = 1$ , i.e. for a particle with twice the design momentum. For a distribution of particles it is particularly convenient to use the dispersion function.

Also quadrupole magnets affect particles differently depending on momentum. The focusing strength of a quadrupole magnet can be expressed as

$$\frac{1}{f} = kl = \frac{l}{B\rho} \frac{\partial B}{\partial x} \quad (4.8)$$

where  $k$  and  $l$  are the quadrupole gradient and the effective length of the magnet,  $B$  the magnetic field strength and  $\rho$  the deflection radius. Since

$$B\rho \propto p = p_0(1 + \delta) \quad (4.9)$$

the focal length of the magnet grows with increasing particle momentum. This is called chromaticity and is illustrated in Fig. 4.1. Normally, this effect is small since the energy spread is small, but in TBL it has a significant effect and requires attention and correction. The correction formalism is treated in Paper III.

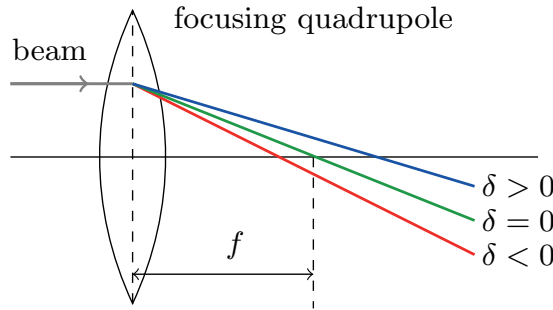


*Figure 4.1.* Illustration of chromaticity in a quadrupole magnet. The focusing of particles with momentum  $\delta < 0$  (red line) shifts towards shorter focal length while it shifts towards longer focal lengths for particles with  $\delta > 0$  (blue line). Only for the design momentum (green line) the focal length is  $f$ .

### 4.3 Acceleration and deceleration

So far we have discussed the guiding system of an accelerator, namely quadrupole and dipole magnets. Now, we will turn to the actual acceleration of the beam. In modern high-energy accelerators we use electromagnetic fields in the radio-frequency (RF) band to accelerate particles. The RF power is fed into accelerating structures or cavities, which are metallic tubes of which the geometry has been optimized to match the particular frequency. Inside the structure, shown in Fig. 4.2, there are geometric obstacles that slow the phase velocity of the electromagnetic wave down to the velocity of the particle so that the RF wave propagates together with the beam and provides continuous acceleration to the particles. The oscillation of the RF wave is synchronized with the arrival time of the bunches in order to guarantee that the particles experience the intended field strength and direction.

An accelerating cavity has a given  $Q$  value, which is defined by the number of oscillation periods that are completed before the amplitude sinks below a given level because of losses in the cavity. Losses occur through the skin effect, where the magnetic field penetrates the walls and causes heating of



the material. Also the beam absorbs power from the structure, called beam loading. Since the structure has a finite filling time, the arrival of the beam is matched to the filling of the cavity so that the beam absorbs a constant amount of power throughout the bunch train. The CLIC drive beam linac will be operated in fully loaded mode, and so is the CTF3 linac [20]. Fully loaded mode is also illustrated in Fig. 4.2 and means that the beam absorbs nearly all of the power that is pumped into the structure. This is a way of maximizing the power efficiency.

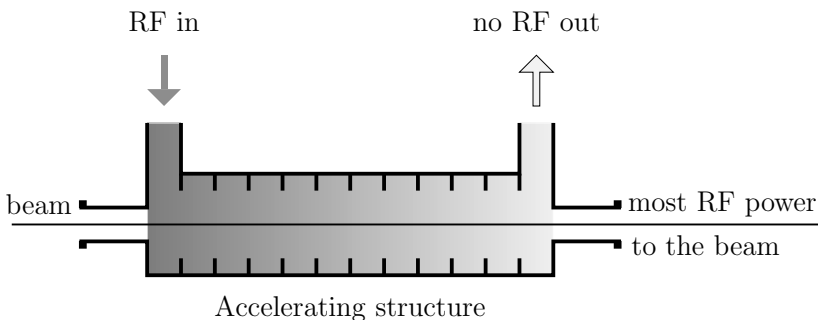


*Figure 4.2.* When an accelerating structure is operated in fully loaded mode it means that the beam extracts almost all the RF power from the structure and that nothing goes to the load. This is the type of accelerating structures used in the CTF3 linac.

The same principle as for particle acceleration can be applied to the deceleration process. In the CLIC decelerator and in TBL we use similar periodically loaded structures, the Power Extraction and Transfer Structures (PETS) [32], to decelerate the beam. They are passive copper structures, that have a fundamental resonant mode frequency of 12 GHz. When the high intensity beam passes through, it leaves a strong wakefield, due to the limited aperture of the structure, which builds up coherently inside the structure. The particles that arrive as a field has been formed, the “witness” particles, leave more of their kinetic energy in the structure, which travels as an RF wave through the structure. So, instead of feeding RF power into the structure, the generated RF wave is coupled out at the end of the structure and extracted. During a short transient time, corresponding to the filling time of the structure, the particles witness a weaker field and suffer no or little deceleration [25]. Following the transient, a steady state arises and most of the bunches along the train, i.e. the largest part of the beam pulse, experience a constant deceleration.

The deceleration is affected by the charge distribution in terms of bunch phase, or arrival time, and the bunch length. We tend to combine these two properties to what is called “form factor” [25], which then represents the coupling of the beam to the field in the PETS. The maximum form factor is 1 and is reached when the bunch frequency is exactly 12 GHz and the bunches are infinitesimally short. In reality, the bunch length is finite and the bunches may be located slightly off in phase, giving a form factor smaller than 1. For a

given bunch length and bunch phase, the deceleration increases linearly with the bunch charge and with the number of bunches in the bunch train.

In TBL, the beam that excites the field in the PETS is bunched at 12 GHz and is decelerated with the same frequency. Given that the bunch length is finite that means that the bunch is long compared to the RF wavelength, which, in turn, means that the particles within a bunch arrives at different phases of the wave. This also implies that different parts of a given bunch experience different fields, which entails a large momentum spread in the decelerated beam. The resulting momentum spread grows with the bunch length and with the number of PETS in the beamline.

This thesis reports on the diagnostics to measure that momentum spread and on development of methods so that conventional diagnostic techniques can be used despite the large momentum spread. The methods used to determine beam profiles are described in the next chapter.

## 5. Beam profile diagnostics

Now that we have seen how we can characterize the beam and the accelerator we will discuss methods to access important beam properties with diagnostics. In this chapter we will go through methods for beam profile monitoring, both transverse profile, i.e. the spatial distribution, and the momentum profile. First we describe how these measurements are normally done. Then, we turn to the special case of monitoring beams with large momentum spread. The technical description of the profile monitors is deferred to chapter 6.

### 5.1 Transverse profile

A low emittance beam, which means the possibility of small beam sizes, is highly desirable at most accelerators, but is rather difficult to create and maintain, which is also why it is important to keep track on the emittance evolution along the accelerator. There are several ways of measuring the emittance and the Twiss parameters in general and we will here describe two of them: a) the quadrupole scan method, and b) multiple screen measurements. They are both based on measuring the horizontal beam size and they assume a thorough understanding of the beamline.

We consider a sector of a beamline that includes at least one quadrupole. At the end of this sector we place a beam size measurement and call it position  $A$ . If the incoming beam is represented by the sigma matrix in Eq. (4.2) we can use Eq. (4.6) to express the beam size  $w_A = \sqrt{\epsilon \beta_A}$  as

$$w_A^2 = R_{11}^2 \sigma_{11} + 2R_{11}R_{12} \sigma_{12} + R_{12}^2 \sigma_{22} \quad (5.1)$$

where  $R_{ij}$  are the elements of the transfer matrix up to  $A$ . The expression in Eq. (5.1) is obtained from the upper left matrix element on respective side in Eq. (4.6). Note that the matrix elements depend on the quadrupole strength and the associated focal length  $f$ . Now, we change the settings of the quadrupole, whereupon the transfer matrix  $R$  changes. This procedure is repeated  $n$  times and a measurement of  $w_i = w_A(f_i)$  is made for every setting. That gives a set of  $n$  equations, linear in the elements of the sigma matrix:

$$\begin{aligned} w_1^2 &= R_{11}^2(f_1) \sigma_{11} + 2R_{11}(f_1)R_{12}(f_1) \sigma_{12} + R_{12}^2(f_1) \sigma_{22} \\ w_2^2 &= R_{11}^2(f_2) \sigma_{11} + 2R_{11}(f_2)R_{12}(f_2) \sigma_{12} + R_{12}^2(f_2) \sigma_{22} \\ &\vdots \\ w_n^2 &= R_{11}^2(f_n) \sigma_{11} + 2R_{11}(f_n)R_{12}(f_n) \sigma_{12} + R_{12}^2(f_n) \sigma_{22}. \end{aligned} \quad (5.2)$$

Assuming that  $R(f_i)$  are known it is now straightforward to invert the system of equations in Eq. (5.2), by first writing it in matrix form

$$\begin{pmatrix} w_1^2 \\ w_2^2 \\ \vdots \\ w_n^2 \end{pmatrix} = \begin{pmatrix} R_{11}^2(f_1) & 2R_{11}(f_1)R_{12}(f_1) & R_{12}^2(f_1) \\ R_{11}^2(f_2) & 2R_{11}(f_2)R_{12}(f_2) & R_{12}^2(f_2) \\ \vdots & \vdots & \vdots \\ R_{11}^2(f_n) & 2R_{11}(f_n)R_{12}(f_n) & R_{12}^2(f_n) \end{pmatrix} \begin{pmatrix} \sigma_{11} \\ \sigma_{12} \\ \sigma_{22} \end{pmatrix}. \quad (5.3)$$

In the ideal case it is enough with  $n = 3$ , i.e. three measurements to extract the three unknowns. In reality, there are measurement errors and uncertainties and the additional measurements are used for solving the equation system Eq. (5.3) in the least-squares sense. Let  $E(w_i)^2$  be the measurement error of the beam width squared,  $w_i^2$ . Solving Eq. (5.3) in the least-squares sense now means minimizing

$$\chi^2 = \sum_i \left( \frac{w_i^2 - R_{11}^2(f_i)\sigma_{11} - 2R_{11}(f_i)R_{12}(f_i)\sigma_{12} - R_{12}^2(f_i)\sigma_{22}}{E(w_i^2)} \right)^2. \quad (5.4)$$

That is equivalent to computing [33]

$$\begin{pmatrix} \sigma_{11} \\ \sigma_{12} \\ \sigma_{22} \end{pmatrix} = (\tilde{M}^t \tilde{M})^{-1} \tilde{M}^t \begin{pmatrix} w_i^2/E(w_i^2) \\ \vdots \end{pmatrix} \quad (5.5)$$

where  $\tilde{M} = \text{diag}(1/E(w_i^2))M$  and  $M$ , with transpose  $M^t$ , is the  $3 \times n$  matrix containing transfer matrix elements in Eq. (5.3). Once the initial sigma matrix elements are known, we can determine the emittances and other Twiss parameters from

$$\varepsilon^2 = \sigma_{11}\sigma_{22} - \sigma_{12}^2, \quad \beta = \frac{\sigma_{11}}{\varepsilon}, \quad \alpha = -\frac{\sigma_{12}}{\varepsilon}. \quad (5.6)$$

Another method for emittance measurements is based on several beam size measurements at different locations in the beamline. As with a quadrupole scan, we can express the beam size  $w_j$  at location  $j$  as in Eq. (5.1). In this case there are several transfer matrices  $R^A, R^B, \dots R^N$ , one for every beam size measurement at the locations  $A, B, \dots N$ . As before we obtain an equation system

$$\begin{pmatrix} w_A^2 \\ w_B^2 \\ \vdots \\ w_N^2 \end{pmatrix} = \begin{pmatrix} (R_{11}^A)^2 & 2R_{11}^A R_{12}^A & (R_{12}^A)^2 \\ (R_{11}^B)^2 & 2R_{11}^B R_{12}^B & (R_{12}^B)^2 \\ \vdots & \vdots & \vdots \\ (R_{11}^N)^2 & 2R_{11}^N R_{12}^N & (R_{12}^N)^2 \end{pmatrix} \begin{pmatrix} \sigma_{11} \\ \sigma_{12} \\ \sigma_{22} \end{pmatrix} \quad (5.7)$$

that we solve as before in Eq. (5.5) with  $M$  taken from Eq. (5.7).

## Chromatic effects in emittance measurements

Note, as a reminder, that the matrix elements  $R_{ij}$  in Eqs. (5.3) and (5.7) depend on the focal length of the quadrupole magnet, and that the focal length varies with beam momentum, coined chromaticity in section 4.2. This means that chromaticity causes the beam envelope to evolve differently than expected if there is a substantial momentum spread in the beam. In Paper III we describe a study of how the large momentum spread can lead to a misinterpretation of the emittance measurements, if we assume a monochromatic beam in the analysis. A quantification of the effect, as well as the remedy, are presented in the paper and are outlined briefly here. Note that this is an effect that appears irrespective of the technique used for transverse beam size measurement, both for quadrupole scans and for several screens in a row.

We consider a thin-lens model of the quadrupole scan emittance measurement setup, which means that we can use the transfer matrices in section 4.2. For now we use a two-by-two matrix and let the momentum variable be present implicitly through the focal lengths. The simplified beam line consists of a quadrupole with nominal focal length  $f_1$ , a drift space of length  $l_1$ , another quadrupole with focal length  $f_2$  followed by a drift of length  $l_2$  and the beam screen. For this analysis we thus need the transfer matrix  $R$  from the first quadrupole to the beam screen

$$\begin{aligned} R &= \begin{pmatrix} 1 & l_2 \\ 0 & 1 \end{pmatrix} \begin{pmatrix} 1 & 0 \\ -1/f_2 & 1 \end{pmatrix} \begin{pmatrix} 1 & l_1 \\ 0 & 1 \end{pmatrix} \begin{pmatrix} 1 & 0 \\ -1/f_1 & 1 \end{pmatrix} \\ &= \begin{pmatrix} 1 - \frac{l_2}{f_2} - \frac{l_1}{f_1} - \frac{l_2}{f_1} + \frac{l_1 l_2}{f_1 f_2} & l_1 + l_2 - \frac{l_1 l_2}{f_2} \\ -\frac{1}{f_1} - \frac{1}{f_2} + \frac{l_1}{f_1 f_2} & 1 - \frac{l_1}{f_2} \end{pmatrix}. \end{aligned} \quad (5.8)$$

Observe that the elements of the transfer matrix  $R$  are functions quadratic in the focal strengths  $1/f_i$ , so that the right hand side of Eq. (5.1) contains up to the fourth power of the inverse focal lengths. Now, we note that the focal length is proportional to the beam energy as stated in Eqs. (4.8) and (4.9), so that it has the momentum dependence

$$\tilde{f}(\delta) = (1 + \delta)f. \quad (5.9)$$

In order to find the momentum dependence of the emittance measurement we augment each focal length  $f$  in Eq. (5.8) with a factor  $1 + \delta$  and insert the new expression for  $R_{ij}$  into Eq. (5.1). We sort the resulting equation into powers of  $1/(1 + \delta)$ . If we have a beam with a momentum distribution  $\psi(\delta)$  we can calculate the rms beam size on the screen  $w$  by averaging over the momentum distribution  $\psi(\delta)$  and we observe that the entire momentum dependence of the beam size is encoded in integrals of the type

$$I_n = \int \frac{\psi(\delta)}{(1 + \delta)^n} d\delta \quad n = 1, \dots, 4 \quad (5.10)$$

where the integral extends over the particle distribution  $\psi(\delta)$ . We can calculate the value of these integrals numerically for almost any momentum distribution  $\psi(\delta)$ . In the analysis of the quadrupole scan measurement, instead of using the monochromatic model as normal, we use the new matrix elements including the chromatic integrals  $I_n$  and thereby avoid any misinterpretation due to large momentum spread.

Further details on the procedure can be found in Paper III.

## 5.2 Momentum distribution

A straightforward way to determine the beam momentum profile is to measure it in a spectrometer line, i.e. in a dispersive section. The position of a particle in a spectrometer line, assuming a dipole field deflection in the horizontal plane, is given by

$$x = x_0 + D_x \delta \quad (5.11)$$

where  $D_x$  is the horizontal dispersion function in the line. For a distribution of particles we obtain the width of the distribution in the spectrometer line through

$$\sigma_x = \sqrt{\varepsilon \beta + \left(D_x \frac{\sigma_p}{p}\right)^2} \quad (5.12)$$

where  $\sqrt{\varepsilon \beta}$  is the geometric beam size in the absence of dispersion. In the spectrometer line the dispersion can be approximated by

$$D_x \approx L \varphi \quad (5.13)$$

where  $\varphi$  is the angle that the spectrometer line makes with the straight line and  $L$  is the total length of the spectrometer arm, from the center of the bend to the location of the beam profile measurement.

The momentum spread of the beam is thus extracted through

$$\frac{\sigma_p}{p} = \frac{1}{D_x} \sqrt{\sigma_x^2 - \varepsilon \beta} \approx \frac{1}{L \varphi} \sqrt{\sigma_x^2 - \varepsilon \beta}. \quad (5.14)$$

The geometric beam size  $w = \sqrt{\varepsilon \beta}$  is best determined by first measuring the Twiss parameters at a location upstream from the spectrometer. Then, we propagate the beta function up to the point of the beam size measurement in the spectrometer line.

### Spectrometry for beams with large momentum spread

Although the dispersion function is defined from a large momentum deviation, Eq. (5.14) is only valid for small momentum spreads. For large spreads it

leads to unphysical results, such as negative momenta. In this case, we need to consider the problem more carefully. We assume a momentum distribution  $\psi(\delta)$ , that enters a spectrometer magnet. The distribution is mapped onto a screen or equivalent in the spectrometer line a distance  $L$  behind the center of the bend, see sketch in Fig. 5.1.

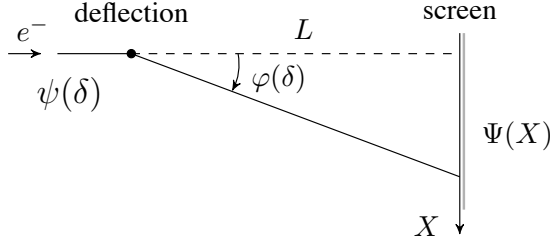


Figure 5.1. Sketch of a horizontal bend followed by a screen.

A particle with initial momentum  $\delta$  will have a final position on the screen  $X \approx L\varphi(\delta)$  where  $\varphi(\delta)$  is the bending angle and

$$X \approx L\varphi(\delta) = \frac{L\varphi_0}{1 + \delta} = \frac{D_0}{1 + \delta}. \quad (5.15)$$

Here, the index 0 refers to the reference momentum particle. The paraxial approximation is recovered by expanding  $1/(1 + \delta)$  in powers of  $\delta$  under the assumption that  $\delta \ll 1$ . We use the relation in Eq. (5.15) to determine the particle density on the screen by integrating over all initial momenta through

$$\Psi(X) = \int \psi(\delta) \delta_D \left( X - \frac{D_0}{1 + \delta} \right) d\delta \quad (5.16)$$

where  $\delta_D$  denotes the Dirac delta function. We start with the integration over  $\delta$  and use the relation

$$\delta_D(g(u)) = \sum_i \frac{\delta_D(u - u_i)}{|g'(u_i)|} \implies \int f(u) \delta_D(g(u)) dx = \sum_i \frac{f(u_i)}{|g'(u_i)|} \quad (5.17)$$

where  $u_i$  are the zeros of  $g(u)$ . In our case,  $g(\delta) = X - D_0/(1 + \delta)$  with one zero at  $\delta_0 = (D_0 - X)/X$  and  $g'(\delta_0) = X^2/D_0$ . The particle distribution on the screen is then given by

$$\Psi(X) = \frac{D_0}{X^2} \psi \left( \frac{D_0 - X}{X} \right) \quad (5.18)$$

where  $X$  is the coordinate on the screen in the bending plane and  $D_0$  is the position on the screen of the reference particle with  $\delta = 0$ . Incidentally,  $D_0$  coincides with the dispersion generated by the dipole.

Normally, we are interested in deducing the momentum profile from the geometric profile on a spectrometer screen. To do so we need the inverted transformation. It is calculated in the same way and reads

$$\psi(\delta) = \frac{D_0}{(1+\delta)^2} \Psi\left(\frac{D_0}{1+\delta}\right). \quad (5.19)$$

For a Gaussian momentum distribution of rms width  $\Delta$ ,

$$\psi(\delta) = \frac{1}{\sqrt{2\pi}\Delta} e^{-\delta^2/2\Delta^2} \quad (5.20)$$

we obtain a particle distribution on the screen

$$\Psi(X) = \frac{1}{\sqrt{2\pi}\Delta} \frac{D_0}{X^2} \exp\left(-\frac{(D_0-X)^2}{2\Delta^2 X^2}\right). \quad (5.21)$$

We see from Eq. (5.21) that the low-energy tail, corresponding to large values of  $X$ , becomes more pronounced on the screen as the spread  $\Delta$  grows larger. Figure 5.2 shows an example with Gaussian momentum distributions with rms widths 5%, 10% and 15%, where the dispersion has been fixed to  $D_0 = 0.3$  m, close to the dispersion at the end of the spectrometer line in TBL. We note that the asymmetry is hardly visible at the smallest spread while quite dominant for the largest spread.

If we analyze the profiles displayed in Fig. 5.2 using the linear approximation  $X \approx D_0(1 - \delta)$ , we will misinterpret the momentum distribution. The extracted peak momentum is shifted down by 0.5%, 1.9% and 4.1%, of respective profile. Depending on how the spread is calculated we will either underestimate or overestimate the spread. For example, a statistical rms gives 1%, 4.3% and a 9.5% overestimation of the reference widths of 5%, 10% and 15% momentum spread. The calculation of the FWHM instead gives a 0.9%, 3.5% and a 7.5% underestimation of the spread.

The situation becomes more critical if we consider the energy distribution at the end of a CLIC drive beam decelerator. The distribution is peaked at 240 MeV but has a long tail that extends all the way up to the maximum energy of 2.4 GeV. If  $p_0 = 240$  MeV,  $\delta$  will reach as high as 10, with the vast majority of the particles within the steady-state, with  $\delta < 4$ . This distribution, projected on a screen with  $D_0 = 0.3$  m, is shown in Fig. 5.3. Again, we use the linear approximation  $X = D_0(1 - \delta)$  to extract the momentum distribution from the screen and obtain the profile shown in Figure 5.4. As a reference, we show also the input momentum distribution, the presence of which highlights that the distribution extracted incorrectly is a severely distorted version of the real. In this example the rms of the reference distribution is 138 MeV while the rms of the extracted distribution is 176 MeV, a 28% overestimation. If we instead calculate the FWHM we get a 160% overestimation of the energy spread. The initial momentum distribution is recovered if Eq. (5.19) is employed for the



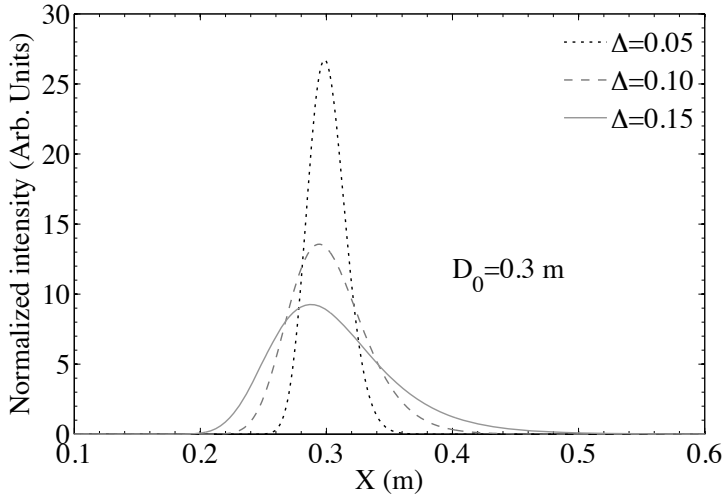


Figure 5.2. A Gaussian momentum distribution becomes asymmetric when projected on a spectrometer screen, if the momentum spread is large.

analysis of the spectrometer profile. Clearly, this is an effect that needs to be taken into account, which is also done in the proposal for time-resolved momentum diagnostics for the CLIC drive beam decelerator in Paper IV and in chapter 7.

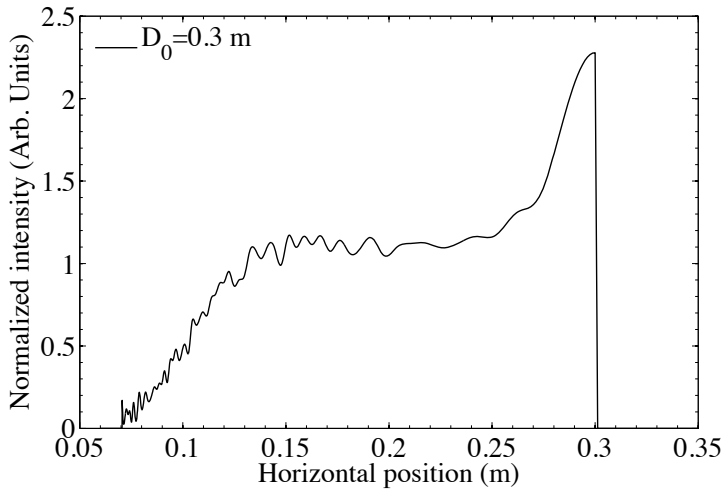
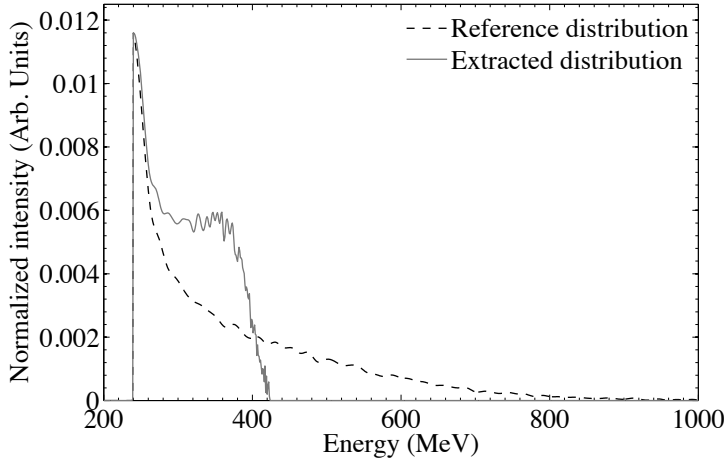


Figure 5.3. The energy distribution at the end of a CLIC drive beam decelerator (see Fig. 2.2) projected on a screen, with  $D_0 = 0.3$  m for  $E_0 = 240$  MeV. The sharp edge corresponds to the beam particles that have experienced maximum deceleration.

In this chapter we have described the standard methods that are used for determining given beam profile parameters, such as the emittances and the



*Figure 5.4.* The dashed line is the reference energy distribution and the solid line is the distribution extracted from the spectrometer measurement in Fig. 5.3 using the normal method, not taking into account the nonlinear dispersion.

momentum spread, from beam size measurements. We also extended these methods to include beams with large momentum spread. The next step is to look at the detectors that we use for these profile measurements. In this area, we have made a contribution by designing, installing and commissioning a device for time-resolved spectrometry. In addition, we have performed a measurement campaign to characterize beam screens in the CTF3 spectrometer lines, documented in Paper V. The result of these efforts is covered in the following chapter.

## 6. Instrumentation

In the previous chapter we looked at diagnostic methods. Here, the technology and the detectors used for beam profile monitoring is discussed.

The monitors discussed in this thesis involve two invasive techniques. The first one measures the induced charge when the charged particles are completely absorbed in a large metallic block. The other is based on the imaging of optical transition radiation (OTR) emitted from a thin foil as the charged particles pass through. We will discuss the underlying physics of the detection techniques and the performance of the instruments, with an overall focus on monitoring large momentum spread beams with or without an intra-pulse time resolution.

The profile measurements in TBL are performed in two separate diagnostic sectors. One is located near the point where the beam enters the CLEX hall, just before TBL, and the other at the end of TBL. These sectors for diagnostics, illustrated in Fig. 6.1, begin with two quadrupole magnets followed by an OTR screen system for transverse profile measurements. This is the equipment used for the quadrupole scans described in section 5.1. Behind the screen system there is a dipole magnet which deflects the beam into the spectrometer line. There, the beam first crosses a second OTR screen, and is finally absorbed in the detector for time-resolved energy measurements. The spectrometer OTR screen provides a high resolution measurement of the momentum spectrum but integrated over the bunch train, while the segmented beam dump provides the intra-pulse temporal information, although at lower resolution.

Paper I describes in detail the design and the characteristics of segmented beam dumps for time-resolved spectrometry. Technical aspects of the OTR screen systems installed in TBL are given in Paper II. Here follows a condensed description of the detector systems.

### 6.1 Segmented beam dump

A segmented beam dump is an array of metallic blocks working as Faraday cups [34, 35]. Placed in the beamline, the beam is stopped in the blocks and the deposited charge is measured as a current flowing to ground through a  $50\,\Omega$  resistance. The process of absorbing a charged particle can be faster than a hundred picoseconds and the overall time-response of the segmented dump has been measured to be below 1 ns, see discussion in Paper I. A segmented dump can therefore be sampled at very short time intervals and thus provide

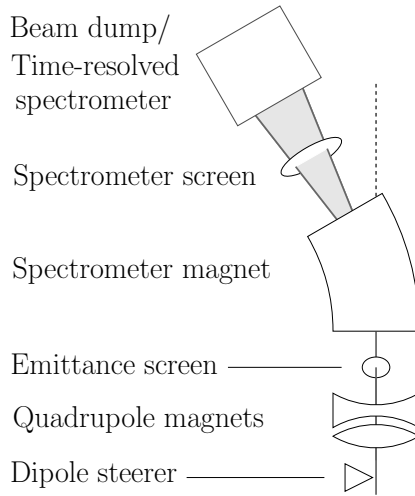


*Figure 6.1.* Sketch of the diagnostic sector in TBL and TL2.

an intra-pulse momentum spectrum. There are four of these devices installed at CTF3 (see e.g. Paper XIII and Ref. [36]), and they have proven to be robust, reliable instruments with great survivability, despite the high radiation levels that degrade the performance of other equipment. A fifth instrument, with a single slit and segment, is installed in the TL2 spectrometer line and provides time-resolved momentum measurements acquired over several beam pulses.

When a charged particle enters a solid block of a given material it interacts with the surrounding atoms and its momentum will gradually decrease. In this case, we only consider electrons as beam particles which means that the electromagnetic interaction is predominant. The electron ionizes atoms in the material by knocking out a bound electron, and thus loses part of its kinetic energy. It also loses energy by emitting bremsstrahlung photons as it is deflected transversely by a nucleus through Rutherford scattering. Depending on the momentum, different processes dominate the retardation of the particle. At low momentum, the electron loses energy mostly due to ionization whereas at high momentum it loses energy through bremsstrahlung. The limit where the two types of energy loss are equally important is called critical energy and lies around 5-15 MeV for most conductors. The photon emitted through bremsstrahlung can have a very high energy and in the presence of nuclei in the material, pair production can occur. These secondary particles also generate showers before they are completely absorbed in the material. There are also other types of scattering, such as photo-nuclear interaction, which can release neutrons, but which are of less importance for beam detection [37].

Through ionization, bremsstrahlung, and Compton scattering of secondary photons, the absorption of one single electron can generate thousands of secondary particles and a wide spread of the charge and energy distribution in

the absorbing block. For the detection of beam particles, it is important that no charge is lost in the process, which means that the block needs to be long enough to fully decelerate the particle longitudinally, and wide enough to contain the shower transversely. In the beginning of the retardation process, the transverse shape of the shower is roughly Gaussian, but the lower the energy of the particle becomes the more likely is it to suffer large angle scattering from a single interaction. The final shower distribution has long tails and is difficult to describe mathematically, since it depends on many parameters such as atomic number of the material, screening effects at different energies, and statistical fluctuations. There are models (see e.g. Molière radius in Ref. [37]) to estimate the geometric distribution of these showers, depending on the material and of the energy of the incoming particle. However, they are complex and require iterative calculations, as the energy of the incoming particle decreases with penetration depth. It is often much more convenient and precise to do a numerical calculation based on Monte Carlo algorithms. There are several simulation tools for this purpose and one of them, FLUKA [38, 39], with the graphical interface Flair [40], was used in the project described here. FLUKA was first developed for radiation dose calculations and is therefore very well suited for simulations of shower evolution in very thick targets, such as a Faraday cup. Figure 6.2 shows an example of the longitudinal projection of the energy deposition in blocks of carbon, tungsten and stainless steel, from an electron beam initially at 200 MeV, simulated with FLUKA. This type of simulations were used to optimize the material and the geometry for the segmented beam dump in TBL. In Paper I, we also compared the results obtained with FLUKA with equivalent simulations made with GEANT4 [41].

With extensive FLUKA simulations the segmented dump design was tailored particularly for TBL. Due to high beam charge tungsten was chosen as segment material. Tungsten has a melting point of over 3400°C and can withstand substantial thermal loads. Moreover, its stopping power is high which reduces the necessary segment dimensions needed to contain the charged particle shower. The geometry of the tungsten segments was optimized to the beam momentum and momentum spread and adapted to the resolution requirements from the large momentum spread beam. In total 32 segments of 3 mm width and 20 mm depth, spaced by 1 mm resulted in a total detector width of 127 mm, which in combination with the 0.35 m dispersion corresponds to an energy acceptance of  $\pm 18\%$ . Despite the resistance to heat, a multi-slit collimator with a high tungsten content was designed to act as a thermal buffer to the system. The 100 mm deep collimator, which is water-cooled, is mounted in front of the segments and absorbs almost the full shower from most of the particles. A small fraction of the beam particles pass through the collimator through 0.4 mm wide slits. The collimator of the segmented dump in the CTF3 linac was designed with parallel slits, as in Fig. 6.3(a). This severely reduced the acceptance of the system (Paper XIII) and was not acceptable for TBL, considering the large momentum spread expected after deceleration. Unlike

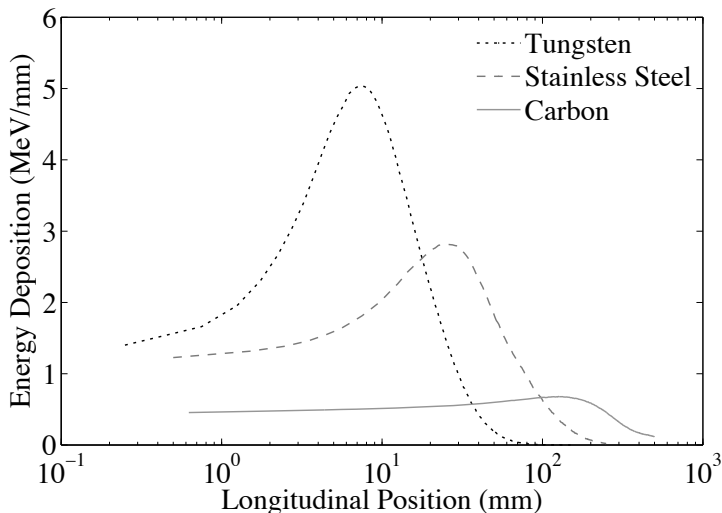


Figure 6.2. Energy deposition integrated over the transverse dimensions, from a 200 MeV electron beam in three materials. The peak and the total range of the shower move deeper into lighter materials.

its predecessors, the TBL segmented dump is therefore equipped with a collimator with radial slits as shown in Fig. 6.3(b), in order to match the divergence of the beam behind the dipole magnet. Acquisition electronics was chosen for intra-pulse sampling of the 140 ns bunch train with 12-bit ADCs at 192 MHz. The sensitive parts of the detector system were made and placed with the dangers of high radiation levels in mind. The progress of the design work was presented in two conference proceedings (Papers XII and XI) and finally summarized in Paper I, together with the description of the other segmented dumps at CTF3.

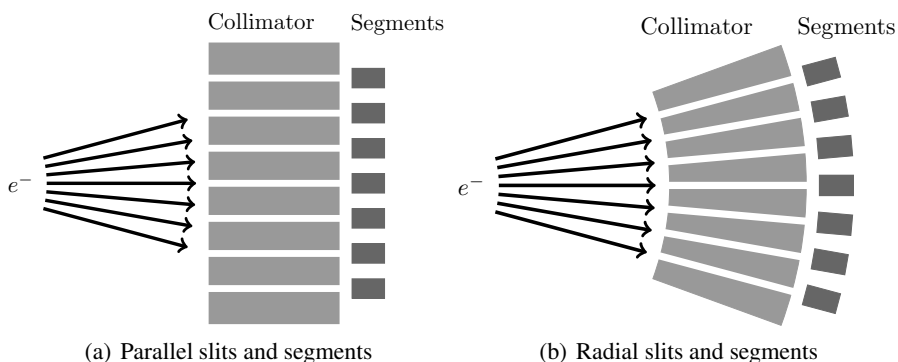


Figure 6.3. Sketch of the geometry of collimator and segments. The radial geometry (b) increases the acceptance of the system compared to the parallel geometry (a). Note that the angles are exaggerated in order to demonstrate the principle.

Before construction, the final design of the segmented dump was tested with FLUKA simulations. The resolution of the system was estimated, taking into account particle crosstalk between segments and the increase of beam divergence from the OTR screen system upstream from the segmented dump. Figure 6.4 shows the result of these simulations, which can be seen as the spatial point spread function of the full detector system. A beam of 150 MeV with negligible cross section was used and the simulations were made in two parts. First, the increase in divergence from the OTR screen system and the vacuum window was estimated. The divergence induced by the foils is equivalent to an rms beam size of  $\sigma_{scatt} = 1.7$  mm at the position of the dump. Second, the particle crosstalk between segments was computed, also using a zero-width beam impinging on the segment in the center. A Gauss fit to the resulting signal amplitudes in all the segments gave an rms width of  $\sigma_{fit} = 2.7$  mm. Adding these numbers in quadrature we obtain the minimum beam width 3.2 mm that can be resolved with the segmented dump. With the 0.35 m dispersion that means a resolution on momentum spread of 0.9%.

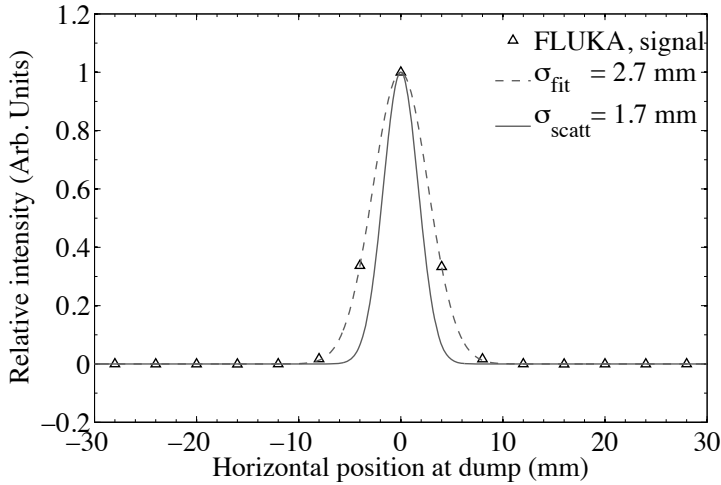


Figure 6.4. FLUKA simulations of the minimum beam width reconstructed from the segmented dump signals. Each point in the FLUKA signal corresponds to one segment. Particle crosstalk between segments contribute by  $\sigma_{fit} = 2.7$  mm and the increase in divergence from the OTR screen, the synchrotron radiation blocker [42] and the vacuum window by  $\sigma_{scatt} = 1.7$  mm.

Also the accuracy of the momentum profile measurement was studied with FLUKA. With the full detector geometry implemented in FLUKA and with an input beam distribution from PLACET simulations, we simulated the beam profile reconstructed from the charge distribution in the segments. The reconstructed profile was compared with the reference PLACET distribution, as shown in figure 12 in Paper II in order to verify that the detector would respond to a realistic beam according to expectations. The reconstructed pro-

file showed a good agreement with the reference profile for various PLACET distributions.

During the commissioning of the segmented beam dump its performance was tested with beam. By integrating the segmented dump measurement over one bunch train, the measurement can be compared with the upstream OTR screen. Figure 14 in Paper II shows two such comparison; one at low beam current and one at high. At low current the deceleration is small and the induced momentum spread is limited. At low current the momentum spread deduced from the OTR screen is smaller than that deduced from the segmented dump, because the resolution of the segmented dump is on the same order as the momentum spread itself. At higher current, however, the momentum spread grows larger and the limited resolution of the segmented dump plays a smaller role. The agreement between the segmented beam dump and the high resolution screen is then improved. From these measurements we conclude that the measured resolution on momentum spread is approximately 1%, which is close to the expected resolution obtained with the FLUKA simulations described above.

The improvement of the momentum acceptance resulting from the radial collimator slits was first tested with simulations, by comparing the reconstructed profile from a system with radial slits with a system with parallel slits (see figure 15 in Paper I). The final result was also tested with beam through a dipole scan method, where the beam is steered across the detector in small steps. We use every segment to reconstruct the beam profile separately and let the amplitude of each profile represent the segment response. Using radial slits proved successful, which is clear from the uniform response of the segments in figure 24 in Paper I.

The measurements described above were performed in order to quantify the performance of the detector. Additional measurements were made for a comparison with other parameters related to the deceleration of the beam. The extracted RF power is measured at every beam pulse with a 1 ns time resolution. From the measurements we can calculate the expected average momentum along each beam pulse and compare the predictions with the segmented dump measurement. Also the beam current, together with an estimate of the form factor, are used for such predictions and comparisons. The segmented dump measurement follows the predictions from RF power production closely, as is shown in figure 17 in Paper II. The prediction from beam current also agrees well with the measured momentum.

Finally, the measured momentum profile was compared with the expected momentum distribution, as simulated with PLACET, shown in Fig. 6.5. First the incoming beam parameters, such as the momentum profile, the emittances, beam intensity and bunch length, are measured. Then, these parameters are used as input to the PLACET simulations of the deceleration process and we obtain a final particle distribution at the end of TBL. The distribution fits well



with the beam profile as measured with the segmented beam dump and the extracted beam width agrees within 3%.

These performance studies are described in detail in Paper II. Because of the good performance of the segmented dump in TBL a copy of the same design will be installed at the end of the CTF3 linac where it will be used for final optimization of the drive beam before the bunch train compression, as is discussed in Paper X.

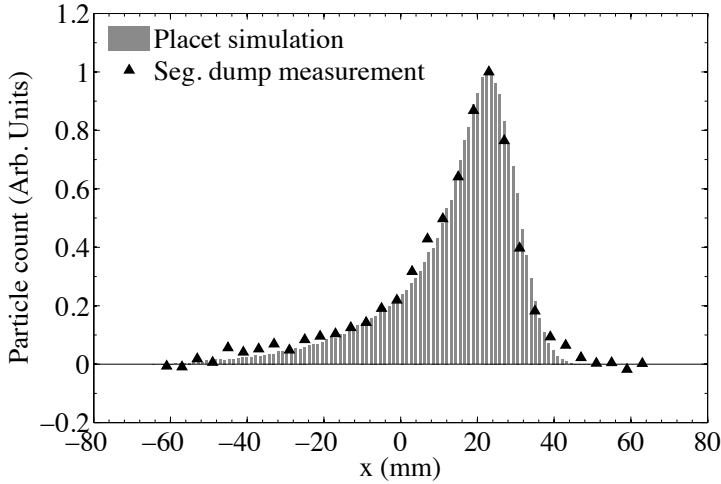


Figure 6.5. The measured beam profile after deceleration in 13 PETS compared to the profile expected from PLACET simulations.

## 6.2 OTR screens

In CTF3, OTR screens are used both for spectrometry and for transverse profile monitoring, where the latter are employed mostly for determining the beam emittance and Twiss parameters through quadrupole scans. Just like the test facility, the OTR screen stations have been added successively and are of different generations. Though, all OTR systems have a similar layout: A vacuum tank containing the OTR screens, an optical line from the view port of the tank to a CCD camera imaging the light emitted in the backward direction. When the beam crosses the screen surface light is emitted from the screen. The light is guided to the camera and the light intensity distribution is related to the particle distribution at the screen. The OTR response time is in the femtosecond range [11], making the camera the temporal bottleneck of the measurement, with its 20 ms acquisition speed.

The systems for transverse profile measurements have a resolution of  $50\text{ }\mu\text{m}$ , and the spectrometer screens  $300\text{ }\mu\text{m}$ , which with the 0.22 m dispersion means better than 0.15% on momentum spread. With another optical system a better

resolution can be obtained. However, that is not required neither for the CLIC nor for the CTF3 drive beam. Details on the hardware and performance on the OTR screen systems are given in Paper II and V.

## Optical Transition Radiation

Optical transition radiation, OTR, was predicted by Ginzburg and Frank in 1945 [11] and first seen experimentally in 1959 by Goldsmith and Jelley [43]. Since then, OTR has found its way into many applications related to particle physics. In accelerators it has been used for beam profile monitoring since the early 1970s, first implemented and developed by L. Wartski [44, 45]. Nowadays, it is widely used, particularly in high intensity electron machines, where scintillating screens cannot be used due to saturation of the light generation process at high current.

Transition radiation is emitted when a charged particle crosses the boundary between two media of different dielectric properties [11]. For beam diagnostic purposes, a thin foil inserted in the beamline is used as an OTR radiator. Placed in the beam path, the beam particle needs to pass through it, passing from vacuum into the radiator material and then back into vacuum. The electric field around the electron polarizes the foil medium, and as the electron passes, the medium relaxes and emits radiation. In this way OTR is emitted both from the entrance and the exit surface. It is conceptually convenient to see the entrance surface as a mirror that reflects the light emitted at the entrance. The emission, or reflection, occurs centered around the specular direction of the radiator and is denoted backward OTR. To facilitate the separation of the OTR from the particle beam it is common to place the radiator at an angle with respect to the beam path. The forward OTR, i.e. the OTR generated as the particles exit the foil, is emitted centered around the beam, see the sketch in Fig. 6.6.

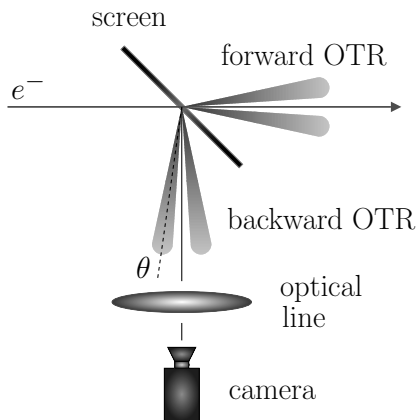


Figure 6.6. Sketch of the OTR emission as the beam passes through the radiating foil.

The angular intensity distribution of the radiation emitted from a perfectly conducting foil can for ultra-relativistic particles with Lorentz factor  $\gamma_r$  and of charge  $q$  be simplified to [46], [44]

$$\frac{d^2W}{d\omega d\Omega} = \frac{q^2}{4\pi^3 \epsilon_0 c} \frac{\theta^2}{(\theta^2 + \gamma_r^{-2})^2} \quad (6.1)$$

where  $\theta$  is the azimuthal angle between the direction of observation and the specular direction, and  $\epsilon_0$  the vacuum permittivity. This means that the intensity is constant over the optical frequencies and is independent of the polar angle  $\phi$ . An example of the intensity distribution is depicted in Fig. 6.7 for beam energies 50 MeV, 100 MeV and 150 MeV.

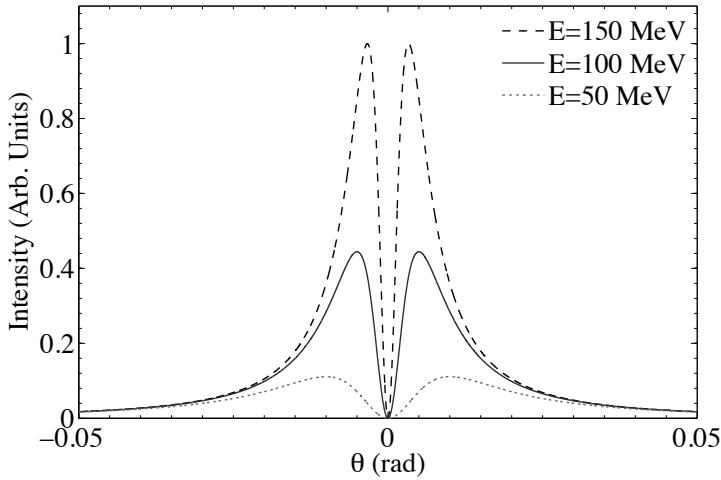


Figure 6.7. Angular distribution of the OTR intensity emitted for beams within the TBL energy range. The intensity peaks at angles  $\pm\gamma_r^{-1}$ .

The angle corresponding to the maximum emission is  $\theta_{max} = 1/\gamma_r$  and is obtained through direct differentiation of Eq. (6.1). Integration of the same equation gives the total number of photons emitted within a frequency range  $[\omega_1, \omega_2]$

$$N = \frac{2\alpha}{\pi} \left( \log(2\gamma_r) - \frac{1}{2} \right) \log \frac{\omega_2}{\omega_1} \quad (6.2)$$

and is presented in the graph in Fig. 6.8 for the energy range covered by the fully decelerated CLIC drive beam. In Eq. (6.2),  $\alpha \approx 1/137$  is the fine structure constant.

From Eq. (6.1) and Fig. 6.7 we note that the average divergence of the emitted light depends on the energy of the incoming particle: The lower the energy, the more wide is the cone of the emitted light. Equation (6.2) describes the energy dependence of the total light emitted. This behavior pose a particu-

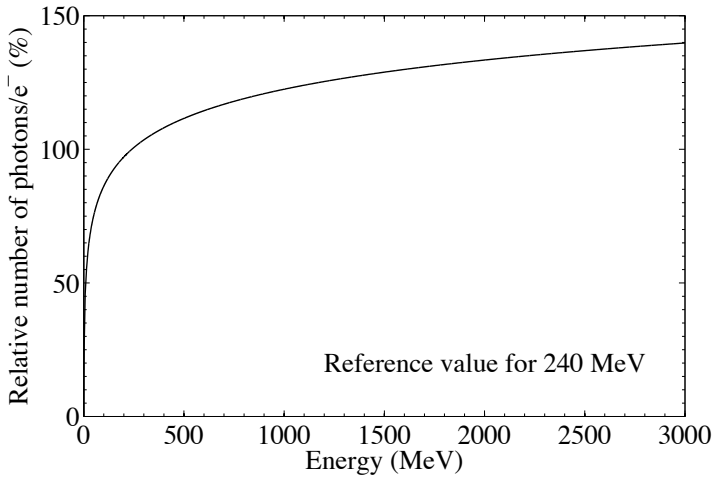


*Figure 6.8.* Relative number of photons emitted per electron in the CLIC decelerator energy range. The most decelerated particle at  $E = 240$  MeV has been used as reference number. At this beam energy an optical photon is emitted per 50 electrons.

lar challenge for OTR-based beam diagnostics, when applied to beams with a large energy spread.

## Momentum effect

The relation between particle energy and the shape and intensity of the emitted OTR can potentially cause problems for imaging beams with large momentum spreads. We have therefore investigated the effect of a large momentum spread on the measured profile by calculating OTR distributions using Eq. (6.2), for beams with the energy distributions expected after strong deceleration. Figure 6.9 shows such a calculation for the steady-state of the fully decelerated CLIC drive beam. We use the peak energy 240 MeV as a reference photon intensity and calculate the relative photon intensity expected at every energy. Here, we assume that a constant fraction of the generated photons are collected. In the figure we see a small discrepancy in the high energy tail but otherwise very little difference between the particle profile and the photon profile. The width of the photon profile, both the rms and the FWHM width, is 3% larger than the particle profile it represents. In Paper II the same issue was addressed for the TBL momentum distribution, with a similar result. This small effect can be eliminated completely by calibrating the screen as the dispersion changes, as described in Paper II.

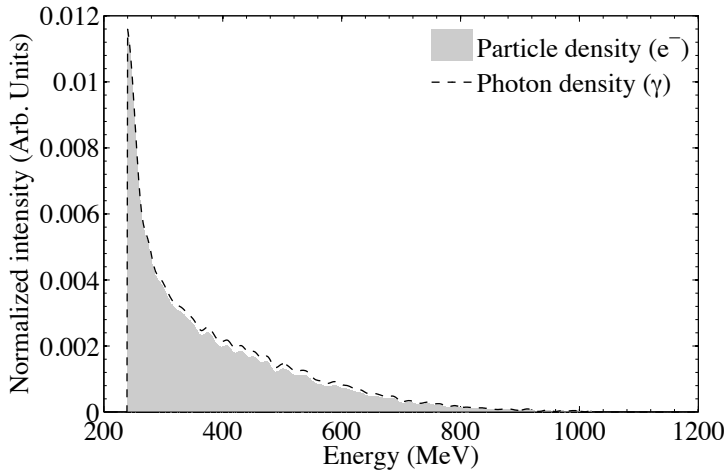


*Figure 6.9.* Energy histogram of the steady-state part of the fully decelerated CLIC drive beam, compared to the OTR density representing the same. The energy dependence of OTR emission, illustrated in Fig. 6.8 lifts the high energy tail slightly, apart from which the distributions are alike.

## Vignetting

A phenomenon well known in ordinary optics and photography is vignetting. It occurs in systems with limited aperture where less light is collected at the edges of the optical system and can lead to dark fringes in a picture, as in the example in Fig. 6.10. An equivalent effect manifests itself in beam imaging. When the beam is large compared to the optical aperture, vignetting leads to distortions of the measured beam profile. The effect is enhanced by the angular properties of OTR as a light source. In contrast to scintillating light, which is an isotropic light source, OTR is highly directional at the emission point, and because of the finite optical aperture, the finite light collection efficiency becomes position-dependent. Furthermore, the angular distribution depends on the beam energy, which is why vignetting is more prominent at high beam energies. It becomes particularly important in spectrometer lines, where the beam is large. In TBL in particular, the large momentum spread results in very large beam widths on the spectrometer screen. In this case, the vignetting would influence the quality of the measurement, if not counteracted.

At CTF3, this problem is reduced through the use of large aperture lenses, with diameter 80 mm. In addition, attempts have been made to counteract vignetting already at the source by modifying the angular distribution of the emitted light. Such a study was initiated at CTF3 in 2006 [48] and included the use of parabolic cylindrical or diffusive OTR targets.

A parabolic cylinder target, with a horizontal curvature that directs the light towards the aperture of the first lens, would overcome the first and most impor-



*Figure 6.10.* An illustration [47] of vignetting in photography. A similar effect occurs in beam imaging.

tant origin of vignetting. With such a screen shape, the light loss is minimized and the position dependence of the light collection is removed.

The method with a diffusive target is based on the opposite principle: The light reflected in the backward direction is diffused at a controlled level, so that the total angular pattern becomes similar to the isotropic case. Thus, the light loss is increased but the position dependence is minimized by ensuring a constant light collection from all points on the screen. That means that less light is collected from particles hitting the screen at the center, whereas light from particles hitting the edge is collected to a higher degree.

In 2011 and 2012 we performed a measurement campaign to characterize all OTR screens at CTF3 and to quantify the vignetting effect. The first part of the study was focused on the spectrometer screens and is the topic of Paper V. The ultimate goal was to determine which of the screen types best mitigates the vignetting effect. The measurements relied on a beam scanning technique, where the beam was steered across the screen in small steps by a dipole corrector magnet. The beam profile on the screen was recorded for every magnet setting and in the off-line analysis of the images, the amplitude and the width of the beam profile were plotted as a function of the beam position on the screen.

In Fig. 6.11 we display the response curve of three screens at CTF3, which is a result of the measurements described above. Here, the response is the

amplitude of the vertical beam profile as a function of the horizontal position of the beam. We use the vertical profile, obtained through integration over the horizontal direction, in order to avoid sensitivity to dispersion, which grows from left to right in the horizontal direction. One of the screens is of the parabolic kind, previously installed in the TL2 spectrometer line. The second screen is a diffusive screen located in the TBL spectrometer line. As a reference, we also display the response of an older screen of the flat, mirror-like type, previously installed at the end of the CTF3 linac. We see that the diffusive screen offers a uniform response over a wide position range. The response of the parabolic screen does not only decrease to 60% of the maximum but is also clearly asymmetric. This result is most likely due to a misalignment of the screen with respect to the optical line. Similar results were obtained with the other systems. Following these results all parabolic screens were replaced with diffusive screens, since the high beam current makes the light intensity less of an issue at CTF3, while more precise screen alignment would require more effort and resources.

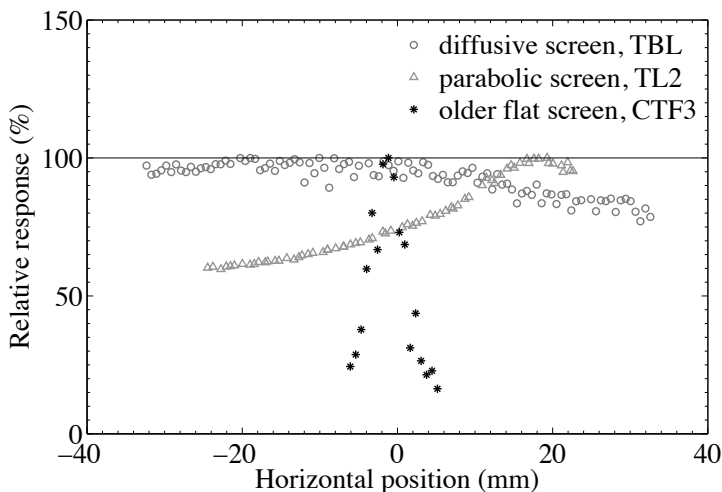


Figure 6.11. The response of OTR screens of various types, measured with a scanning method.

From Paper II we conclude that the existing beam diagnostics for profile measurements are well adapted to the TBL beam characteristics. Remember, though, that however large the momentum spread in TBL is, it is small compared to the expected spread at the end of a CLIC drive beam decelerator. Moreover, the total beam power will be many times higher, which rules out the use of segmented beam dumps for time-resolved momentum measurements. With extra attention paid to the effect of high beam power in combination with invasive instruments, the use of OTR screens may still be an option. In order

to access the intra-pulse information of the beam profile we need to modify the measurement set-up completely. This is the topic of chapter 7.



## 7. The post-PETS line

The analysis of the beam profile diagnostics in TBL in Papers I and II has shown that segmented beam dumps, currently used for time-resolved spectrometry in TBL, are not suitable for the CLIC decelerators due to the high beam power. On the other hand, OTR screens have a good chance of surviving the high intensity. We therefore intend to base the time-resolved measurements of transverse and energy profile in the CLIC decelerator on OTR screens. The general layout envisioned for the diagnostics is to have two scanning kicker magnets sitting in the same place in the beamline: One kicking in the vertical direction, and the other in the horizontal direction, similarly to the dilution kickers forming the figure “e” of the beam on a screen in the LHC dump line [49]. We assume that the kickers can be excited in a cycle corresponding to the 240 ns drive beam duration and with a rise of the magnetic field that provides a kick from zero to a few milliradians in the same time range. Furthermore, we assume that the magnet excitation can be made in a way that the horizontal kicker is driven by a cosine wave while the vertical is driven by a sine wave, thus making it possible to form a Lissajous figure of the beam on the screen. Forming the sweep into a circle allows us to analyze the momentum distribution along the beam pulse. A linear sweep in one direction at a time gives information about the transverse beam distribution along the pulse.

We will begin with a prediction of what will be seen on the screen for a given beam distribution in time and momentum when the circular sweep is applied. Later, we will show examples of the measurement and of the analysis. Paper IV contains a detailed description of the method and presents examples for which the quality of the measurement analysis has been studied

### 7.1 Time-resolved spectrometry

In order to establish a way of extracting time-resolved information from the spectrometer measurement we first look at how a particle distribution transforms when projected onto a screen. We use the variables defined in Fig. 5.1 and introduce a rotating effective magnetic field vector so that a particle with momentum  $\delta$  hits the screen at the coordinates

$$X = \frac{L\varphi_0 \cos(2\pi\tau)}{1 + \delta}, \quad Y = \frac{L\varphi_0 \sin(2\pi\tau)}{1 + \delta} \quad (7.1)$$

with  $\tau = t/T$  where  $T$  is the period of the magnetic cycle and  $0 < \tau < 1$ . Let further  $\psi(\tau, \delta)$  be the initial particle density distributed over time and

momentum. We ignore for now the emittance and obtain the transverse particle distribution on the screen  $\Psi(X, Y)$  by integrating over time and momentum through

$$\Psi(X, Y) = \iint \psi(\tau, \delta) \delta_D\left(X - \frac{L\varphi_0 \cos(2\pi\tau)}{1 + \delta}\right) \delta_D\left(Y - \frac{L\varphi_0 \sin(2\pi\tau)}{1 + \delta}\right) d\tau d\delta. \quad (7.2)$$

We use the Jacobi determinant to transform the integration variables from  $(\tau, \delta)$  to  $(X, Y)$  and obtain the final result

$$\Psi(X, Y) = \frac{L\varphi_0}{2\pi} \frac{1}{(X^2 + Y^2)^{3/2}} \psi\left(\frac{1}{2\pi} \arctan\left(\frac{Y}{X}\right), \frac{L\varphi_0}{\sqrt{X^2 + Y^2}} - 1\right). \quad (7.3)$$

We now turn to extracting the original time dependent momentum distribution  $\psi$  from an image produced by the rotating magnetic field on the screen. For this we need to invert the procedure and determine the original time dependent momentum distribution  $\psi(\tau, \delta)$  from the distribution on the image  $\Psi(X, Y)$ . The inverse procedure starts similarly with a two-dimensional integral, which, after variable substitution, results in

$$\psi(\tau, \delta) = \frac{2\pi (L\varphi_0)^2}{(1 + \delta)^3} \Psi\left(\frac{L\varphi_0 \cos(2\pi\tau)}{1 + \delta}, \frac{L\varphi_0 \sin(2\pi\tau)}{1 + \delta}\right). \quad (7.4)$$

The momentum information is now encoded in the radial variable on the screen and the temporal information is in the angle. We refer to Paper IV for the detailed derivations.

Our goal is to perform these measurements on the decelerated CLIC drive beam, and therefore we show it in Fig. 7.1. We have used the momentum distribution of the steady-state part of the pulse and let the momentum profile be constant along the bunch train in Fig. 7.1(a). By applying Eq. (7.3) we obtain the corresponding screen image in Fig. 7.1(b). The head of the pulse is located to the lower right and the end of the pulse at the upper right part of the image. As was already seen in Fig. 5.3, the high energy tail is compressed so that the intensity is lifted at the center of the screen.

For the evaluation of the performance we have chosen a particle distribution whose momentum along the pulse varies sinusoidally with amplitude  $\delta = 0.1$ . The assumed rms momentum spread  $\Delta$  has the same magnitude. This momentum distribution, shown in Fig. 7.2(a), results in an image on the screen shown in Fig. 7.2(b). Here, we have neglected the effect of finite emittance. In the simulation we assume a deflection angle  $\varphi_0 = 1$  mrad for the reference particle ( $\delta = 0$ ) and drift length  $L = 5$  m. Using the procedure outlined above to extract the momentum distribution from the image indeed results in a distribution that is indistinguishable from the one shown in Fig. 7.2(a).

A finite emittance will smooth out the profile on the screen. If the geometric beam size on the screen is known the screen image can be corrected through

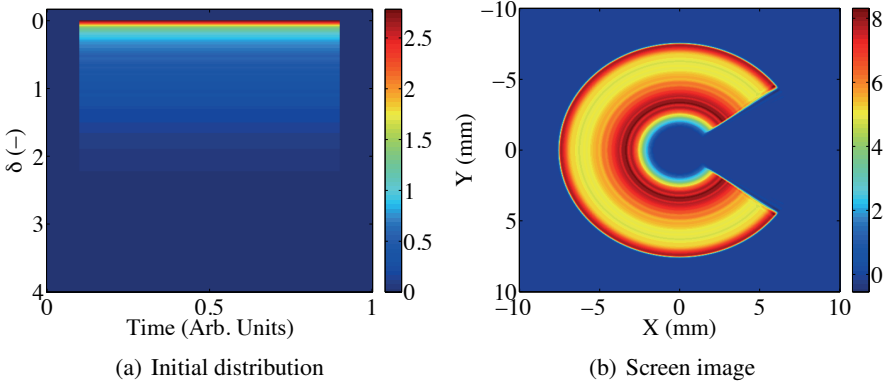


*Figure 7.1.* The CLIC momentum distribution transformed to an image in the post-PETS diagnostic line. We have used  $L = 5$  m and  $\phi_0 = 1$  mrad. The head of the pulse, corresponding to the time  $\tau = 0.1$ , is in the lower right corner.

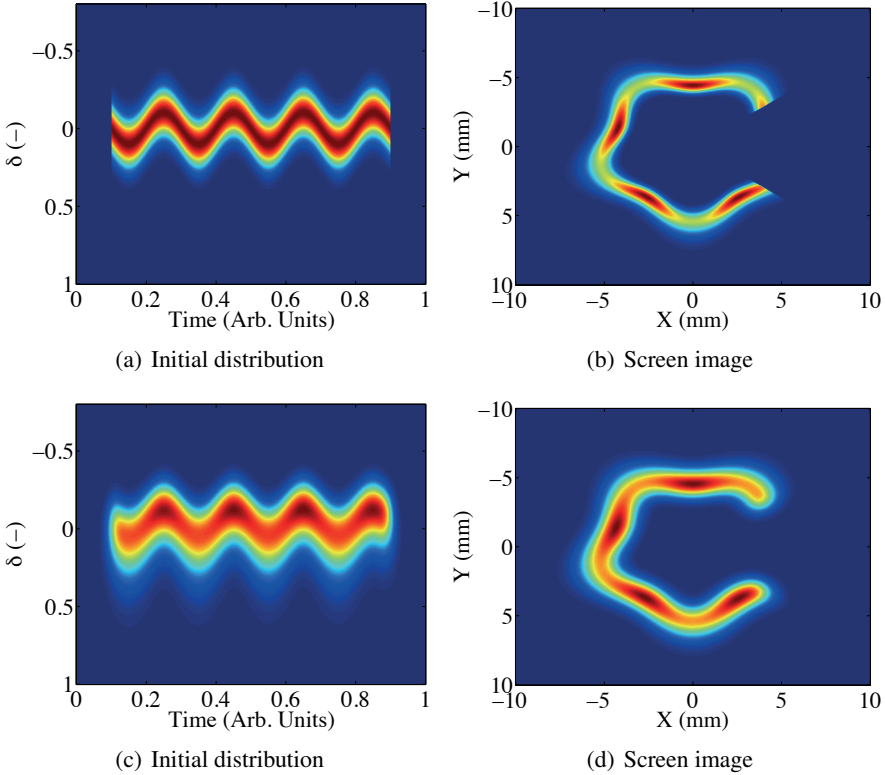


*Figure 7.2.* Reference distribution (a) and screen image (b). The momentum spread is 0.1 along the pulse while the average momentum oscillates with an amplitude equal to the rms spread. In (d) the original image in (a) has been convoluted with a geometric beam size that represents a finite emittance. Extracting the momentum profile from the image (d), without taking the finite emittance into account, gives the distribution in (c).

deconvolution with the geometric beam profile. This, however, requires careful use of advanced image processing and here we limit the analysis of the effect of a finite emittance to a qualitative level. In Fig. 7.2(c) we demonstrate the effect of a finite emittance by calculating the convolution of the original screen image from Fig. 7.2(b) with the geometric beam profile. In Fig. 7.2(d) we have used a geometric beam size equal to the beam size due to the momentum spread. We note that qualitative information can be extracted from the screen even though the emittance is large, with the general trend that the extracted momentum spread increases with increasing emittance, while the extracted average momentum decreases.

In the CLIC decelerator the finite emittance is not expected to influence the measurement notably since the momentum spread is so large that even with a very small dispersion the geometric beam size will be negligible in comparison. In the next section we will discuss the beam size measurements, which can be used also for emittance measurements.

## 7.2 Time-resolved beam size measurements

For time-resolved beam size measurements in one plane, say horizontal, we envision to make a linear sweep in the other, here vertical, direction. Variations in the horizontal beam size along the pulse will then show up as variations of the horizontal width of the image on the screen, where time along the pulse is encoded in the vertical position. One horizontal slice of the image thus corresponds to the horizontal profile of a given temporal slice in the pulse. A large momentum spread, however, will cause vertical smearing out of particles from one temporal slice across neighboring temporal slices. In this way the large momentum spread entangles the momentum and beam size distributions. Note that this smearing out is more complex than plain convolution, because it depends on the deflection angle and therefore varies along the pulse. Instead of solving this image processing problem, we perform simulations to investigate to what extent beam size variations can be resolved, even in the presence of large momentum spread.

We demonstrate the beam size measurement with the example in Fig. 7.3. A beam pulse with a variation of the horizontal beam size along the pulse is introduced. The vertical beam size is assumed to be negligible in Fig. 7.3 compared to the Gaussian momentum distribution, of which the rms spread  $\Delta$  is 0.05. The vertical smearing of the horizontal distribution of a given temporal slice is due to spreading of the momentum distribution, transformed according to Eq. (5.18) to the image plane. Figure 7.3(a) shows the image on the screen and Fig. 7.3(b) the rms beam size in the horizontal plane along the pulse, extracted from the image to the left. The modulation that we used as input to the simulation is also shown, and we observe that the oscillations are damped by the smearing from the momentum spread. Simulations like these were performed

for increasing momentum spread and the standard deviation of the oscillations along the pulse calculated for every momentum spread. The standard deviation, shown in Fig. 7.4, decreases rapidly with increasing momentum spread and eventually approaches zero. After this point, the method does not reveal any temporal variations of the horizontal beam size. We conclude that for moderate momentum spread the method provides some qualitative information about the horizontal beam size, but is limited if the momentum spread becomes too large.

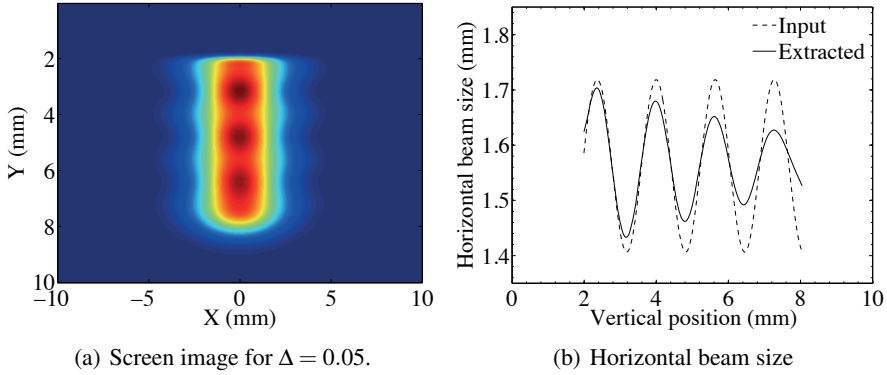


Figure 7.3. Image of a beam with momentum spread  $\Delta = 0.05$  and a variation in horizontal beam envelope along the pulse (a). The rms horizontal beam width along the pulse, equivalent to the vertical axis, is displayed in (b). The first bunch is centered at approximately  $Y = 2$  mm and the last bunch at  $Y = 8$  mm.

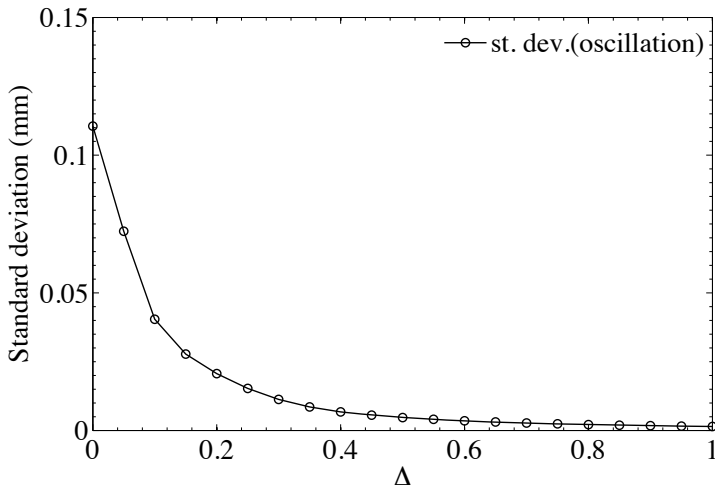
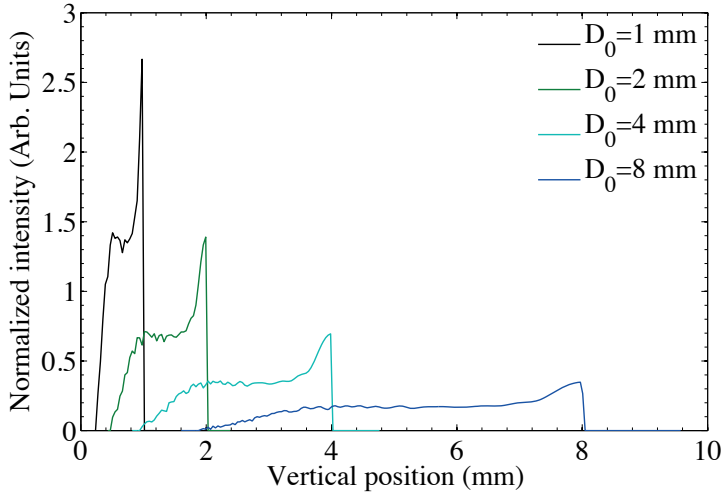


Figure 7.4. Standard deviation of the extracted variation of the horizontal beam size along the pulse, as a function of the momentum spread  $\Delta$ .

Finally, treating a beam with CLIC parameters, we apply, as before, a linear sweep in the vertical direction. Figure. 7.5 illustrates how the momentum profile is extended in the vertical direction of the screen for different deflection angles, corresponding to different points in time during the sweep. The later bunches are superimposed with the early bunches, which highlights the difficulty of extracting quantitative time information from the image. By extracting the rms beam size, as explained above, we can still identify modulations of the beam size along the pulse even on the decelerated CLIC drive beam, albeit on a qualitative level only.



*Figure 7.5.* The CLIC momentum distribution in the vertical plane for selected deflection angles  $\varphi_0 = D_0/L$ . Every angle corresponds to a point in time during the sweep, where the sweep begins with a small deflection angle and ends with a large angle. The large spread leads to contamination from the late bunches of the regions where the early bunches are imaged.

## 8. Conclusion

The candidate for a future electron-positron collider CLIC relies on a unique two-beam accelerations scheme, where a high intensity drive beam is decelerated in order to provide acceleration power for the main beam, thus using a particle beam as a distributed high-power RF source. As the drive beam is decelerated its momentum spread grows, which is a challenge for beam stability and beam transport. A test beam line, TBL, has been constructed at CERN to study the transport of the decelerated beam during power extraction. This thesis reports on novel methods and instruments for the beam profile measurements necessary to optimize and characterize the performance of the drive beam decelerator.

We have designed, installed and commissioned a segmented beam dump for time-resolved momentum measurements of the decelerated drive beam in TBL. The detector provides the intra-pulse momentum spectrum with 1% resolution on momentum spread and 5.2 ns sampling time. Compared to previous models of the same detector type, the performance is improved. In particular, the momentum acceptance has increased through a geometry of the detector that matches the divergence of the beam. The segmented dump has been compared, with good agreement, to another device installed in the same spectrometer line, which provides an integrated measurement of the momentum profile. The segmented dump measurements also agree with predictions from extracted RF and with beam simulations.

OTR screens are used in TBL for transverse and momentum profile measurements, averaged over the bunch train. One of the problems with imaging large beams with screens, as is the case in the spectrometer lines, is vignetting. Different methods for counteracting vignetting were investigated and through large optical apertures and diffusive screens the problem is removed. The energy dependence of OTR is easily compensated for on spectrometer screens.

The chromatic effect in the quadrupole magnets lead to beam sizes that differ significantly from the beam sizes expected for a monochromatic beam. When the momentum spread in the beam is large, emittance measurements through quadrupole scans need to follow a specialized routine. The model used for analyzing the quadrupole scan measurement and for extracting the emittance from the beam size measurements must be corrected for the large momentum spread, something that can be done numerically. With this modified analysis method the quadrupole scan is interpreted correctly.

Extending the diagnostics in TBL to the CLIC decelerator, the post-PETS instrumentation beamline is proposed for time-resolved spectrometry in the

CLIC decelerators. In the post-PETS line, a rotating magnetic deflection disperses the beam in a circular shape on an OTR screen, thus providing the momentum information in the radial direction and the time stamp through the polar angle along the circle. Qualitative beam size measurements along the bunch train will be made through a linear rise of the deflection in one transverse direction at a time. By reducing the variation of the beam envelope in the other transverse direction the machine can be tuned.



## 9. Sammanfattning på svenska

Titeln på den här avhandlingen lyder i direktöversättning: *Emittans- och energidiagnostik för elektronstrålar med stor rörelsemängdsspridning*. Den berör forskning kring att utveckla och utvärdera mätinstrument som undersöker egenskaper hos partikelstrålar i en framtida linjär partikelkrossare. Syftet med forskningen är att finna tillförlitliga metoder att mäta eftersökta egenskaper, i det här fallet emittans och energifördelning, för att i slutändan optimera prestandan hos partikelkrossaren. Partikelkrossaren i sin tur är ett verktyg i sökandet efter universums minsta beståndsdelar och grundläggande krafter.

### Partikelfysik och partikelkrossare

Vi människor har i alla tider varit nyfikna på världen omkring oss. Vi studerar och funderar med målet att förstå hur allt hänger ihop, vad vi består av och hur allt började. I fysiken, läran om naturen, ligger forskningens fokus på att finna grundläggande lagar för materiens struktur och rörelse. Genom experiment vill man kunna återskapa fysikaliska processer under kontrollerade former i syfte att så noggrant som möjligt kartlägga samband och företeelser.

Partikelfysikens metoder går ut på att leta efter universums grundläggande byggstenar och mäta hur alla byggstenar, eller partiklar, hänger ihop, hur de interagerar med varandra. Därmed vill vi kunna förutse fysikaliska processer. Under de senaste decennierna har partikelfysiker varit mycket upptagna med att bekräfta giltigheten hos Standardmodellen, en av de mest populära modellerna för att beskriva världen och dess minsta beståndsdelar. Standardmodellen är som ett stort pussel där varje elementarpartikel har en särskild plats. Det visar sig dock att pusslet inte är komplett, att modellen inte kan användas för att beskriva och förutse alla kända fysikaliska fenomen. Arbetet med att utöka Standardmodellen med kompletterande teorier fortskrider därför.

Partiklarna som partikelfysiker letar efter är mycket små och ofta mycket ”tunga”. För att se det lilla behövs kort våglängd – lika kort som eller kortare än storleken på objektet i fråga. Att nå ner till korta våglängder motsvarar att komma upp i stora energier. Man använder redan kända partiklar som man låter kollidera med varandra i hopp om att skapa en tredje partikel. Partikelkrossare där två partikelstrålar möter varandra är det mest effektiva sättet att uppnå stor energi och därmed att utforska nya områden i partikelfysikpusslet.

I dag är LHC den största partikelkrossaren i världen. Här krockar man två protonstrålar vid mycket stor energi. I själva verket består protonerna av kvarkar och det är i kollisionen mellan kvarkar som nya partiklar uppstår. Bundna

i protonen har kvarkarna en inbördes energifördelning och man kan därför inte veta exakt vid vilken kollisionenergi som den nya partikeln bildades. För det krävs att man krockar elementarpartiklar. Elektroner och deras antipartiklar positroner är de enklaste elementarpartiklarna att bilda strålar av och dessa vill man därför använda i framtidens partikelkrossare för precisionsmätningar.

Det finns två huvudgrupper av partikelkrossare: linjära och cirkulära. Partikelstrålarna accelereras genom att de "surfar" på elektromagnetiska radiofrekvensvågor och de hålls på plats i acceleratoren med hjälp av magnetfält. När en laddad partikel böjs av från sin bana, till exempel när den av starka magnetfält tvingas att göra en cirkulär rörelse, så svarar den genom att skicka ut så kallad synkrotronstrålning. Synkrotronstrålningen innebär en energiförlust som är större för lätta partiklar, såsom elektroner, än för de tyngre protonerna. För att undvika denna energiförlust väljer man att utveckla en linjär partikelkrossare. Linjära accelerators blir väldigt långa om partiklarna ska kunna nå stor energi innan de kolliderar. Mycket forskning och utveckling sker på området med framtida linjära kolliderare där elektroner kollideras med positroner. En betydelsefull kandidat till en sådan framtida anläggning heter CLIC, vilket står för Compact Linear Collider.

## CLIC, CTF3 och TBL

CLIC är tänkt att bli en i sammanhanget kompakt linjärkolliderare. Detta ska åstadkommas genom att man accelererar partiklarna med en stor gradient, eller accelerationsgrad, det vill säga att partiklarna suger åt sig mycket energi i förhållande till den sträcka de färdas. Sådan acceleration blir mest energieffektiv om man använder en högfrekvent radiofrekvensvåg för att accelerera partiklarna. Denna våg ska i sin tur genereras av att en annan partikelstråle, den så kallade drivstrålen, bromsas. Drivstrålen har speciella egenskaper i form av mycket hög intensitet och bildas genom komplicerade metoder för att omvandla ett långt tåg av partikelbuntar till ett kortare tåg där buntarna ligger tätare. När drivstrålen färdas genom speciellt utformade metallrör lämnar den efter sig en del av sitt omgivande elektriska fält i form av elektromagnetiska vågor. Dessa vågor matas ut ur inbromsningsapparaturen och leds till liknande metallrör i vilka huvudstrålen sedan accelereras till mycket stor energi. På så vis utgör drivstrålen en kraftkälla till huvudstrålen som kan omfördelas dit där den behövs.

När drivstrålen bromsas in tappar den följaktligen stora delar av sin energi. Samtidigt ökar energispridningen eftersom alla partiklar inte tappar samma mängd energi. Det är svårt att hålla en sådan stråle stabil. Den stora energispridningen leder till att strålen växer betydligt i storlek så att den så småningom riskerar att gå förlorad genom att partiklar krockar med den omgivande utrustningen. För att undvika detta krävs att partikelstrålens egenskaper övervakas så att motaktioner kan sättas in. Detta görs med stråldiagnostik, det

vill säga instrument och metoder utvecklade för att mäta olika egenskaper hos partikelstrålen som helhet. Jag har arbetat med att utveckla diagnostiska instrument för profilmätningar, det vill säga strålens geometriska utbredning. I en spektrometerlinje, efter att strålen har passerat en dipolmagnet, kan den rumsliga utbredningen översättas till en energifördelning eftersom partiklarna avlänkas olika beroende på sin energi eller rörelsemängd. Sådan energifördelning, samt emittans, som är ett begrepp kopplat till strålens rumsliga fördelning, är de profil-mätningar jag främst har arbetat med.

CLIC är ett stort projekt som kräver detaljerade förstudier innan det kan sättas i verket. I syfte att bevisa att det föreslagna dubbelstrålekonceptet fungerar så har en testanläggning byggts på CERN. Denna testanläggning, CLIC Test Facility 3, förkortat CTF3, har bekräftat att den intensiva drivstrålen kan skapas så som föreslagits. Där undersöks också processen med att accelerera en stråle med hjälp av kraften hämtad från drivstrålen. Uppsala Universitet medverkar i den studien genom att ha byggt instrumentuppställningen och genom löpande bidrag och stöd till CTF3. Även beteendet hos drivstrålen då den har lidit kraftig energiförlust studeras vid CTF3. Den sistnämnda studien äger rum i TBL, Test Beam Line, och är den strållinje vid vilken jag har arbetat med profil-mätningar av den inbromsade strålen.

## Strålfilm-mätningar

Jag har arbetat med mätningar av två nyckelparametrar hos strålen. Mätningarna av dessa, emittans och energiprofil, baseras båda på mätningar av den geometriska partikelfördelningen i genomskärning. Dessa har genomförts med två tekniker för stråldetektering: en segmenterad Faraday-kopp samt OTR-skärmar, skärmar som skickar ut optisk övergångsstrålning, Optical Transition Radiation.

En elektron omges av ett elektriskt fält. När partikeln i hög hastighet närmar sig och slutligen passerar gränsen till ett annat material så påverkas laddningsfördelningen i materialet av det elektriska fältet. Materialet polariseras så att de bundna elektronerna i materialet flyttar sig längre ifrån den korsande elektronen medan de positiva laddningarna attraheras. När elektronen har passerat nollställs polarisationen och laddningsfördelningen återgår till den ursprungliga. Den energi som har överförts via polarisationen sänds då ut som elektromagnetisk strålning. Då många elektroner passerar i form av en stråle så avges tillräckligt mycket strålning i det optiska spektrat för att vi ska kunna fånga det på bild med en kamera. Ljusets fördelning återspeglar då strålens utbredning och vi får en profil-mätning. En sådan profil-mätning kan göras både då strålen går rakt fram och då den böjs av i en spektrometerlinje. Därmed kan vi med OTR mäta både den inneboende geometriska fördelningen och energifördelningen hos strålen. Dock begränsar kameran den frekvens med vilken vi kan utföra mätningarna. Den tid det tar att läsa av kameran motsvarar den tid

det tar för många partikelbuntar att passera, vilket gör att vi med den metoden endast kan avläsa medelvärdet av fördelningen och inte hur den förändrar sig längs med en följd, eller ett tåg, av partikelbuntar.

För en sådan tidsupplöst mätning av energifördelningen används en segmenterad Faraday-kopp. En Faraday-kopp består av ett block av ett ledande material som placeras i vägen för strålen. Koppen stoppar elektronerna i strålen, vilket ger ett överskott av negativ laddning i materialet. Det överskottet vandrar sedan som en elektrisk ström till en jordad punkt och kan därmed läsas av som en elektrisk signal. Eftersom det går snabbt att stoppa elektronerna och för den elektriska signalen att fortplanta sig så kan detektorn läsas av så ofta som varje nanosekund, det vill säga varje miljarddels sekund. Eftersom ett tåg av partikelbuntar är några hundra nanosekunder långt kan signalen som skapas av strålen läsas av längs med tåget. Att Faraday-koppen är segmenterad innebär att detektorn består av 32 plattor placerade bredvid varandra som läses av var och en för sig. Varje platta absorberar elektroner och därmed får vi en bild av hur utbredd partikelstrålen är.

I avhandlingen och tillhörande artiklar har jag undersökt prestanda och kvalitet hos dessa detektorer och tillhörande mätmetoder. Tyngdpunkten har legat på att mäta egenskaper hos strålar som har stor energispridning, då detta påverkar hur detektorn svarar på strålen och därmed hur vi tolkar mätningarna. Jag har arbetat med att ta fram en ny modell av den segmenterade Faraday-koppen, särskilt anpassad till strålen i TBL. Med hjälp av strålmätningar har jag konstaterat att den nya modellen fungerar enligt förväntningarna. Den förser oss med ett tidsupplöst spektrum av strålen som överensstämmer med den närliggande OTR-skärmen, med mätningar av den extraherade kraften samt med vad vi förväntar oss utifrån simuleringar av energifördelningen efter inbromsningen. Denna utrustning används kontinuerligt och är ett viktigt redskap i studierna av vad som händer när drivstrålen bromsas upprepade gånger.

Medan den segmenterade Faraday-koppen fungerar utmärkt i TBL så kommer den inte att överleva länge i CLIC. TBL är ett test i liten skala av motsvarande inbromsningsanläggning i CLIC och strålintensiteten i den slutgiltiga maskinen kommer att vara mycket högre. Detta innebär större mekaniska och termiska påfrestningar än vad detektorn beräknas klara av. Istället har vi föreslagit att OTR-skärmar används i en ny uppställning. Genom att ha ett tidsberoende magnetfält så att strålen sprejas på skärmen i en cirkel kan vi komma åt energifördelningen genom ljusfördelningen i radiell ledd på skärmen och tidsaxeln genom vinkeln i förhållande till en referensaxel. På så sätt får vi ett tidsupplöst energispektrum, vars upplösningsförmåga beror på skärmstorlek och avlänkningsvinkel. Med samma skärm kan vi även skaffa oss en kvalitativ bild av hur strålstorleken förändras längs med partikeltåget genom att vi använder en avlänkning som ökar linjärt längs med tåget i en riktning i taget, horisontell eller vertikal.

Den mängd ljus som avges från OTR-skärmen beror på vilken energi partikeln som orsakar emissionen har. Även utbredningen av det utsända ljuset

förändras med partikelenergin. Detta innebär att även om den geometriska fördelningen hos strålen är densamma så kan den bild vi uppfångar se annorlunda ut om partiklarna har en och samma energi jämfört med om de har stor energispridning. Den effekten har vi undersökt för spektrometerskärmar och har konstaterat att effekten är liten. Den lilla effekten är även enkel att korrigera.

Den stora energispridningen påverkar också hur strålen beter sig längs acceleratoren och vid inbromsningen. Partikelstrålens storlek varierar längs med acceleratoren och begränsas genom att den fokuseras av magneter. Men eftersom magnetfält avläskar partiklar i proportion till deras energi så förändras partikelstrålens storleksvariation med dess energiinnehåll. När vi fastställer strålens emittans så gör vi det baserat på upprepade strålstorleksmätningar för olika fokuseringsstyrka hos en eller flera magneter. Den stora energispridningen leder till att vi misstolkar mätningarna. I avhandlingen finns en metod beskriven för att ta den uppmätta energifördelningen i beaktan för att korrigera emittansmätningen. Denna metod kommer att vara betydelsefull vid strålinbromsaren i CLIC.



## 10. Abbreviations and acronyms

<b>ATLAS</b>	A Toroidal LHC Apparatus
<b>ALICE</b>	A Large Ion Collider Experiment
<b>BPM</b>	Beam Position Monitor
<b>CCD</b>	Charge-coupled Device
<b>CERN</b>	European Organization for Nuclear Research, originally named <i>Conseil Européen pour la Recherche Nucléaire</i>
<b>CLEX</b>	CLIC Experimental Area
<b>CLIC</b>	The Compact Linear Collider
<b>CMS</b>	Compact Muon Solenoid
<b>CR</b>	Combiner Ring
<b>CTF3</b>	The CLIC Test Facility 3
<b>DL</b>	Delay Loop
<b>ECFA</b>	European Committee for Future Accelerators
<b>FODO</b>	Focusing Defocusing
<b>FWHM</b>	Full Width at Half Maximum
<b>IP</b>	Interaction Point
<b>LEP</b>	Large Electron-Positron Collider
<b>LHC</b>	Large Hadron Collider
<b>LHCb</b>	Large Hadron Collider beauty
<b>Linac</b>	Linear accelerator
<b>MSSM</b>	Minimal Supersymmetric Extension of the Standard Model
<b>OTR</b>	Optical Transition Radiation
<b>PETS</b>	Power Extraction and Transfer Structure
<b>PHIN</b>	Photo Injector
<b>rms</b>	Root mean square
<b>RF</b>	Radio-frequency
<b>SM</b>	Standard Model
<b>SUSY</b>	Supersymmetry
<b>TBL</b>	The Test Beam Line
<b>TBTS</b>	The Two-Beam Test Stand
<b>TL2</b>	Transfer Line 2





# Acknowledgements

It all started more than six years ago when I took a course in subatomic physics at the University of Gothenburg, and our lecturer Göran Nyman, professor at Chalmers, brought the whole class to CERN for a study visit. I was amazed by the expensive machinery, the miles and miles of cables and the walls of blinking computers, the mountains, the chaos in the canteens and the many nationalities coming together in one place of work. Göran encouraged me to apply for the Summer Student Program at CERN and eventually I was accepted. That was the beginning of my path into accelerator physics, CERN and research. Thank you, Göran, for spreading your enthusiasm!

I have had the privilege of working with many people during these past four years and I have had teams of coworkers spread over three countries: The BI group and in particular the PM section in France, the CLIC/CTF3 team, mostly in Switzerland, and my university colleagues in Uppsala, Sweden. The geographical spread is even bigger when I count all my friends and family, which means that there are people from every continent who, in one way or another, have contributed to my work with this thesis. Some have offered scientific guidance or just general support and advice on technical details. Some have fed me, entertained me and shared the load of everyday life. Others have just supported me with their friendship. Although, I would like to thank everyone by name, I have made a careful selection of people or groups of people who have played an extra big role in my life for the last few years.

I am so grateful to have had you, Volker, as my PhD supervisor. You have been a great support in many matters. You have encouraged and inspired me by seeing a solution to every problem. You have helped me prioritize and you have taught me to trust my gut feeling. Above all, you remind that we do physics because it's fun and that it's fun because it's difficult. Thanks for guiding me all the way to the end!

My CERN supervisors Thibaut and Enrico: Thank you for helping me juggle many tasks in a challenging and colorful work environment!

Anne and Daniel - two very important members of the dump family: I learned a lot and had a lot of fun working with you!

All my colleagues in the BI/PM section at CERN: Thank you for all the coffee

breaks and all the other things we shared! You all deserve big Thanks/Merci beaucoup/Grazie mille/Hartelijk dank. I have met many other friendly faces in BI and at CERN. Honorable mentions to the members of the BLM and the ML sections.

Thank you to the CLIC team in general and the CTF3 gang in particular. It's been messy, but it's been fun! A special thank you to the CTF3 operators and to my colleagues at TBL: Erik, Steffen and Reidar.

My research project was supported by a Marie Curie ITN Fellowship under contract number (PITN-GA-2008-215080-DITANET). I want to thank DITANET for employing me and for introducing me to the beam diagnostics community, Tom for also being in DITANET, the European Commission for funding the project and Uppsala university, through Tord Ekelöf, for accepting me as a PhD student. Lastly, I owe big thanks to CERN for hosting me and my fellowship for three years.

My colleagues in Uppsala: Andrea! Having you struggling with your PhD project in parallel with my own struggle has been a great way of relieving me of some of the pressure. Thanks also to my other office mate Marek, who is always helpful and who never complains when I sing in the office. Thank you Roger, for continued support both at CERN and in Uppsala! The rest of the fika group: Gergana, Mathias, Rocio, Niklas, Marek, Masih, Rolf, Lars: You made my return to Sweden a piece of cake! (Note that this was an unintentional play on words.) Not to forget all of you PhD and Master's students, and other more senior colleagues, who have made lunches, coffee breaks and karaoke sessions a true pleasure.

Three very important people who have helped me with a lot of things: Inger Ericson, Madeleine Catin and Glenda Wall. Without you I would probably be stranded somewhere in the world with an invalid visa or flight ticket.

Members of my various temporary families during my years at CERN: The Nordic-Italian family with Tiina, Mario, Pietro and Alberto. Thank you for the food and the lovely company! I swear it wasn't me who washed the moccia brewer. The German family: Toni and Alex. Whenever you have news to share.... The Cuban family: Yisel. Short but no less memorable. The chosen family: Nicol and Yann. Choosing you as my flat mate(s) was one of the best decisions I have ever made. The Swedish family: Karin and Tess. When nobody else could understand me.

Friends in Geneva: Georgios, Alex, Leo, Valerio, Octavio, Camilla, Samir, Matias, Josh, Juha, Antonella, Christoph, Serena, Cesar, Tiia, Michi, Silvia, ...and many more. Much thanks to you there was never a dull moment.

My GU buddies: Johan, Christer, Tomas, Hannes, Malle, Emmanuel, Micke, Gustav, Matias, Bengt. Those years when we studied physics together will always be the period when I laughed the most, and I wouldn't be here today if it wasn't for you.

Friends from yore, who always deserve to be remembered and thanked in the warmest possible way. Although we meet each other less often these days, I still see you as my best friends, Josefin, Amanda, Joar, Karin, and Anna!

Thanks a million to all aunts, uncles and cousins for being so funny and supportive, and for calling me brave and smart! Perhaps extra thanks to Julia, Toby and Ester with whom I spent a lot of time before leaving Gothenburg for CERN.

Now, a few more people who deserve individual thanks:

Anna Hellstrand: I have come to depend on our talks over the last few years. Encouragement, consolation, and the occasional sermon have made it possible for me to struggle on and to grow as a person. This summer it's my turn to go visit you!

Julia Winroth, my partner in crime: You are an inspiration to me and I admire you for sailing through life, dodging all the lethal rocks, and never taking anything for granted. I'm your fan. Thank you for being mine!

Georgios "Gorgeous" Konstantinou: Thank you for cheering for me until the very end. Your comradeship means the world to me.

Karin Ulin: You are the cream cheese to my bagel, and often you even provide the bagels. I want to put it here so that everyone can see it: Du är bäst! DU! Keep spreading your wisdom, and please, keep returning back home in between missions!

I also take this opportunity to thank my adopted family members over the world: Kumiko, come visit us soon! We miss you. Mãe Cândida, pai José Luíz, maninha Rachel, e avó Lacy: Estão sempre no meu coração!

Slutligen ett stort, varmt tack till min närmaste familj: Tack för att ni finns! Mamma Gerd och pappa Anders: Måtte ni njuta ordentligt av er tid som pensionärer nu när jag äntligen slutar skolan! Varmaste tack till världens bästa storsyster Sara, världens bästa Pål och världens bästa systerson Allan, för allt stöd genom åren. Att få en ny familjemedlem var helt klart den största och mest fantastiska händelsen i mitt liv hittills. Jag ser fram emot att bli Allans älsklingsmoster och hoppas att jag kan träffa er ofta.



# References

- [1] P. W. Higgs. Broken symmetries, massless particles and gauge fields. *Physics Letters*, 12(2):132–133, 1964.
- [2] L. Bergström. Non-baryonic dark matter: observational evidence and detection methods. *Reports on Progress in Physics*, 63(5):793, 2000.
- [3] S. Abachi et al. Observation of the top quark. *Phys. Rev. Lett.*, 74:2632–2637, Apr 1995. (D0 Collaboration).
- [4] F. Abe et al. Observation of top quark production in  $\bar{p}p$  collisions with the collider detector at Fermilab. *Phys. Rev. Lett.*, 74:2626–2631, Apr 1995. (CDF Collaboration).
- [5] G. Aad et al. Observation of a new particle in the search for the Standard Model Higgs boson with the ATLAS detector at the LHC. *Physics Letters B*, 716(1):1 – 29, 2012. (ATLAS collaboration).
- [6] G. Aad et al. Search for charged Higgs bosons decaying via  $H^\pm \rightarrow \tau\nu$  in  $t\bar{t}$  events using  $pp$  collision data at  $\sqrt{s} = 7$  TeV with the ATLAS detector. *Journal of High Energy Physics*, 2012:1–50, 2012. (ATLAS collaboration).
- [7] The  $\mu^+\mu^-$  collider collaboration. Muon muon collider: A feasibility study, Jun 1997. BNL-52503; Fermi Lab-Conf.-96/092; LBNL-38946.
- [8] C. M. Ankenbrandt et al. Status of muon collider research and development and future plans. *Phys. Rev. ST Accel. Beams*, 2:081001, Aug 1999.
- [9] European Committee for Future Accelerators. Report of the working group on the future of accelerator-based particle physics in Europe, September 2001. ECFA/01/213.
- [10] E. Coniavitis and A. Ferrari. Pair production of heavy MSSM charged and neutral Higgs bosons in multi-TeV  $e^+e^-$  collisions at the Compact Linear Collider. *Phys. Rev. D*, 75:015004, Jan 2007.
- [11] John David Jackson. *Classical electrodynamics*. Wiley, New York, 3. edition, 1999.
- [12] Klaus Wille. *The physics of particle accelerators: an introduction*. Oxford University Press, Oxford, 2000.
- [13] H. H. Braun et al. CLIC 2008 parameters, Oct 2008. CLIC-Note-764.
- [14] E. Chevallay, M. Csatari, A. Dabrowski, S. Doebert, D. Egger, V. Fedosseev, O. Mete, M. Olvegaard, and M. Petrarca. PHIN photo-injector as the CLIC drive beam source. *Journal of Physics: Conference Series*, 347(1):012036, 2012.
- [15] A. Ferrari, V. Ziemann, R. B. Appleby, and M. D. Salt. Conceptual design of a beam line for post-collision extraction and diagnostics at the multi-TeV Compact Linear Collider. *Phys. Rev. ST Accel. Beams*, 12:021001, Feb 2009.
- [16] H. Braun, J.-P. Delahaye, A. De Roeck, and G. Geschonke. CLIC here for the future. *CERN Courier*, Sep 2008.
- [17] A multi-TeV linear collider based on CLIC technology: CLIC conceptual design report, 2012. CERN-2012-007.

- [18] H. Braun, J.-P. Delahaye, G. Geschonke, G. Guignard, K. Hübner, and I. H. Wilson. R and D for the feasibility study of CLIC technology, Aug 2004. CLIC-Note-596.
- [19] G. Geschonke and A. Ghigo. CTF3 design report, May 2002. CERN-PS-2002-008-RF; CTF-3-NOTE-2002-047; LNF-2002-008-IR.
- [20] R. Corsini et al. First full beam loading operation with the CTF3 linac. In *Proceedings of EPAC 2004, Lucerne, Switzerland*, Aug 2004. CERN-AB-2004-057.
- [21] P. Skowronski, S. Bettoni, R. Corsini, A. E. Dabrowski, S. Döbert, A. Dubrovskiy, F. Tecker, R. Ruber, C. Biscari, and W. Farabolini. Progress towards the CLIC feasibility demonstration in CTF3. In *Proceedings of IPAC'10, Kyoto, Japan*, pages 3410–3412, Jun 2010. CLIC-Note-826.
- [22] W. Farabolini et al. Two beam test stand experiments in the CLEX CTF3 facility. In *Proceedings of IPAC 2011 conference, San Sebastián, Spain*, pages 29–31, 2011.
- [23] A. D. Yeremian, R. Miller, R. D. Ruth, H. H. Braun, G. Geschonke, L. Groening, L. Rinolfi, L. Thorndahl, I. H. Wilson, and F. Zhou. CTF3 drive-beam injector design. In *Proceedings of EPAC 2002, Paris, France*, pages 527–529, Sep 2002. CLIC-Note-542.
- [24] A. Palaia, M. Jacewicz, R. Ruber, V. Ziemann, and W. Farabolini. Effects of rf breakdown on the beam in a CLIC prototype accelerator structure, 2013. Submitted to Phys. Rev. Spec. Top. AB, arXiv:1301.4673.
- [25] E. Adli. *A Study of the Beam Physics in the CLIC Drive Beam Decelerator*. PhD thesis, University of Oslo, Oslo, Norway, 2009.
- [26] E. Adli, A. E. Dabrowski, S. Döbert, R. Lillestøl, M. Olvegård, D. Schulte, and I. Syratchev. Experimental program for the CLIC Test Facility 3 test beam line. In *Proceedings of IPAC'10, Kyoto, Japan*, pages 4410–4412, 2010.
- [27] F. Toral et al. Design, manufacturing and tests of a micrometer precision mover for CTF3 quadrupoles. In *Proceedings of EPAC08, Genoa, Italy*, pages 1517–1519, 2008.
- [28] D. Schulte. PLACET: a program to simulate drive beams. In *Proceedings of EPAC 2000, Vienna, Austria*, pages 1402–1404, Jul 2000. CERN-PS-2000-028 AE.
- [29] D. Schulte. The tracking code PLACET, Sep 2005. <https://savannah.cern.ch/projects/placet/>.
- [30] R. Q. Twiss and N. H. Frank. Orbital stability in a proton synchrotron. *Review of Scientific Instruments*, 20:1–16, 1949.
- [31] E. D. Courant and H. S. Snyder. Theory of the alternating-gradient synchrotron. *Annals of Physics*, 3:1–48, Jan 1958.
- [32] I. Syratchev, D. Schulte, E. Adli, and M. Taborelli. High RF power production for CLIC. In *Proceedings of PAC07, Albuquerque, New Mexico, USA*, pages 2194–2196, 2007. CERN-AB-2007-059; CLIC-Note-720.
- [33] W. Press, B. Flannery, S. Teukolsky, and W. Vetterling. *Numerical Recipes*. Cambridge University Press, 1987.
- [34] K. L. Brown and G. W. Tautfest. Faraday cup monitors for high-energy electron beams. *Review of Scientific Instruments*, 27(9):696–702, 1956.
- [35] M. Rosing, C. Hummer, and R. Zolecki. The measurement of Twiss parameters

- using segmented Faraday Cups. In *Proceedings of the 1989 IEEE Particle Accelerator Conference, Chicago, Illinois, USA*, pages 1586–1588, 1989.
- [36] T. Lefèvre, C. Dutriat, E. Bravin, and H. H. Braun. Segmented beam dump for time resolved spectrometry on a high current electron beam. In *Proceedings of DIPAC 2007, Venice, Italy*, pages 340–342, 2007. CERN-AB-2007-030-BI; CLIC-Note-729.
- [37] W.-M. Yao. Review of particle physics. *Journal of Physics G*, 33:1+, 2006. (Particle Data Group).
- [38] G. Battistoni, F. Cerutti, A. Fasso, A. Ferrari, S. Muraro, J. Ranft, S. Roesler, and P. R. Sala. The FLUKA code: Description and benchmarking. *AIP Conf. Proc.*, 896(SLAC-REPRINT-2007-184):31–49. 19 p, 2007.
- [39] A. Ferrari, P. R. Sala, A. Fasso, and J. Ranft. *FLUKA: A multi-particle transport code (program version 2005)*. CERN, Geneva, 2005. CERN-2005-10; INFN/TC\_05/11; SLAC-R-773.
- [40] V. Vlachoudis. Flair: A powerful but user friendly graphical interface for FLUKA. In *Proceedings of the Int. Conf. on Mathematics, Computational Methods & Reactor Physics (M&C 2009), Saratoga Springs, New York, U.S.A. (2009)*, 2009.
- [41] S. Agostinelli et al. Geant4 - a simulation toolkit. *Nuclear Instruments and Methods in Physics Research Section A: Accelerators, Spectrometers, Detectors and Associated Equipment*, 506(3):250 – 303, 2003.
- [42] T. Lefèvre, C. Bal, H. H. Braun, E. Bravin, S. Burger, R. Corsini, S. Döbert, C. Dutriat, F. Tecker, P. Urschütz, and C. P. Welsch. Time resolved spectrometry on the CLIC test facility 3. In *Proceedings of EPAC 2006, Edinburgh, Scotland*, pages 1205–1207, Jul 2006. CERN-AB-2006-079; CLIC-Note-685; CTF3-Note-080.
- [43] P. Goldsmith and J. V. Jelley. Optical transition radiation from protons entering metal surfaces. *Philosophical Magazine*, 4(43):836–844, 1959.
- [44] L. Wartski, J. Marcou, and S. Roland. Detection of optical transition radiation and its application to beam diagnostics. *IEEE Transactions on Nuclear Science*, 20(3):544–548, 1973.
- [45] L. Wartski, S. Roland, J. Lasalle, and G. Filippi. Interference phenomenon in optical transition radiation and its application to particle beam diagnostics and multiple scattering measurements. *J. Appl. Phys.*, 46(8):3644–3653, 1975.
- [46] K. Honkavaara. *Optical Transition Radiation in High Energy Electron Beam Diagnostics*. PhD thesis, Helsinki Institute of Physics, Helsinki, Finland, 1999.
- [47] H. Taavola. Lejon på vägg, 2013.
- [48] C. P. Welsch, E. Bravin, and T. Lefèvre. Optimization of OTR screen surface materials and OTR screen geometry at CTF3. *Rev. Adv. Mater. Sci*, 16:73–79, 2007.
- [49] B. Goddard, R. Riffaud, M. Sans-Merce, and W. Weterings. Conceptual design of the LHC beam dumping protection elements TCDS and TCDQ. In *Proceedings of EPAC 2004, Lucerne, Switzerland*, pages 629–631, Aug 2004. LHC-Project-Report-756; CERN-LHC-Project-Report-756.

# Acta Universitatis Upsaliensis

*Digital Comprehensive Summaries of Uppsala Dissertations  
from the Faculty of Science and Technology 1036*

Editor: The Dean of the Faculty of Science and Technology

A doctoral dissertation from the Faculty of Science and Technology, Uppsala University, is usually a summary of a number of papers. A few copies of the complete dissertation are kept at major Swedish research libraries, while the summary alone is distributed internationally through the series Digital Comprehensive Summaries of Uppsala Dissertations from the Faculty of Science and Technology.



ACTA  
UNIVERSITATIS  
UPSALIENSIS  
UPPSALA  
2013

Distribution: [publications.uu.se](http://publications.uu.se)  
urn:nbn:se:uu:diva-198080